doi:10.26443/seismica.v5i1.1818

A new global P-wave tomographic model of the Earth's mantle

Guust Nolet [1,2], **Sébastien Bonnieux** [1], **Yongshun J. Chen** [3], **Yann Hello** [1], **Kasra Hosseini** [4], **Yuko Kondo** [5], **Dalija Namjesnik** [1], **Masayuki Obayashi** [6], **Karin Sigloch** [1], **Joel D. Simon** [2,8], **Frederik J. Simons** [2], **Inna Slezak-Oreshina** [1,9], **Hiroko Sugioka** [5], **Junko Yoshimitsu** [6], **Yong Yu** [7]

[1]Université Côte d'Azur/CNRS/OCA/IRD, Géoazur, Sophia Antipolis, 06560, France, [2]Department of Geosciences, Princeton University, Princeton, NJ 08544, USA., [3]School of Ocean Science and Engineering, SUSTech, 518055, Shenzhen, China, [4]Zalando SE, [5]Kobe University, Kobe, Japan, [6]Research Institute for Marine Geodynamics, JAMSTEC, Yokosuka 237-0061, Japan, [7]State Key Laboratory of Earthquake Dynamics and Forecasting, Institute of Geology, China Earthquake Administration, Beijing 100029, China., [8]Now at: Bathymetrix, LLC, Portland, OR 97202, USA, [9]Now at: Observatoire de la Côte d'Azur, Laboratoire Lagrange (Université de la Côte d'Azur/CNRS)

Author contributions: *Conceptualization, methodology and software*: Guust Nolet. *Data acquisition*: All authors. *Writing - Original draft*: Guust Nolet. *Writing - Review & Editing*: All authors.

Abstract We have inverted a very large combination of delay times for P, pP, PcP, PKPab, PKPbc from the ISC-EHB catalog, augmented with hand-picked OBS and MERMAID onset data and cross-correlation delays from broadband stations to derive a new global model, UNICA25, of P-wave velocity variations in the mantle. This paper presents the model, summarizes the data processing and inversion, and shows resolution tests at different scales. After rejecting 109 917 outliers (1% of the total), the data set comprises 10 571 152 arrival times. The misfit of the observed delays, with respect to a background model consisting of the crust of LITHO1.0 on top of model AK135, is on average 2.14 standard errors (σ), which is reduced to 0.99σ by inverting for P-wave velocity variations using both ray theory and finite frequency theory, and 5000 iterations of the iterative solver LSQR. Extensive resolution tests show a resolution at 500 km scale or better in most of the lower mantle. An upper mantle resolution of the order of 300 km is obtained under densely instrumented continents, but upper mantle resolution remains deficient under much of the oceans except where covered by MERMAIDs. Linearized tomography is at least three orders of magnitude faster than recent full waveform inversions (FWI), and reaches much higher frequencies for cross-correlated delays. Model UNICA25 has a P-velocity resolution that rivals that of FWI and shows a superior performance in fitting delay times, notably the ISC-EHB P-delays.

Production Editor: Yen Joe Tan
Handling Editor: Suzan van der Lee
Copy & Layout Editor: Sarah Jaye Oliva

Received: July 9, 2025
Accepted: March 5, 2026
Published: April 8, 2026

1 Introduction

Global seismic tomography has come a long way since the pioneering attempt by Dziewonski et al. (1977) to map P-velocity anomalies in the mantle by inverting delay times published at the time in the Bulletin of the International Seismological Centre or ISC (Adams et al., 1982). Contrary to S-wave tomography which is dominated by surface wave and normal mode inversions, and more recently by low-frequency full waveform inversions, P-wave tomography has benefitted substantially from first arrival time picks that can be very precise, and that offer the sharp sensitivity afforded by ray theory. Certainly in subduction zone regions with dense seismic arrays and high rates of seismicity down to almost 700 km depth, considerable progress has been made in mapping downgoing slabs.

Slabs have the additional advantage of having positive velocity anomalies, which are less prone to the effects of wavefront healing (Nolet and Dahlen, 2000) and are therefore easier to image than negative anomalies if only ray theory is used. Using ray theory, van der Hilst et al. (1991) and Spakman et al. (1993) were the first to show that slabs penetrate the lower mantle in the NE Pacific and the Mediterranean, respectively. Somewhat controversial at first, this finding is now well accepted, and discussion has shifted to monitor the fate of slabs once they enter the lower mantle (Fukao and Obayashi, 2013; Obayashi et al., 2013). However, even among fairly recent tomography models, large differences in images persist, as is evident from Fig. 1 which shows two slabs, subducting beneath the Phillipines and the Mariana Islands, as imaged by five different high-resolution tomography efforts. The two models in the left column of this figure, UU-P07 (Amaru, 2007; Hall and Spakman, 2015) and TX2019slab-P (Lu et al., 2019) are based on travel-time picks only. PRI-P05 (Montelli et al., 2004, 2006) was the first model to combine picks with cross-correlation delays, which require finite-frequency kernels (Dahlen et al., 2000) to be modelled. The difference between ray-theoretical delays and finite-frequency (dispersive) delays yields information on the size of anomalies along the raypath. Models GAP-P4 (Obayashi et al., 2013) and DETOX-P3 (Hosseini et al., 2020) represent more recent applications of this combined approach. The cross-section in Fig. 1 was chosen because it is not dominated by information of locally very dense seismic arrays. It may be a poor case

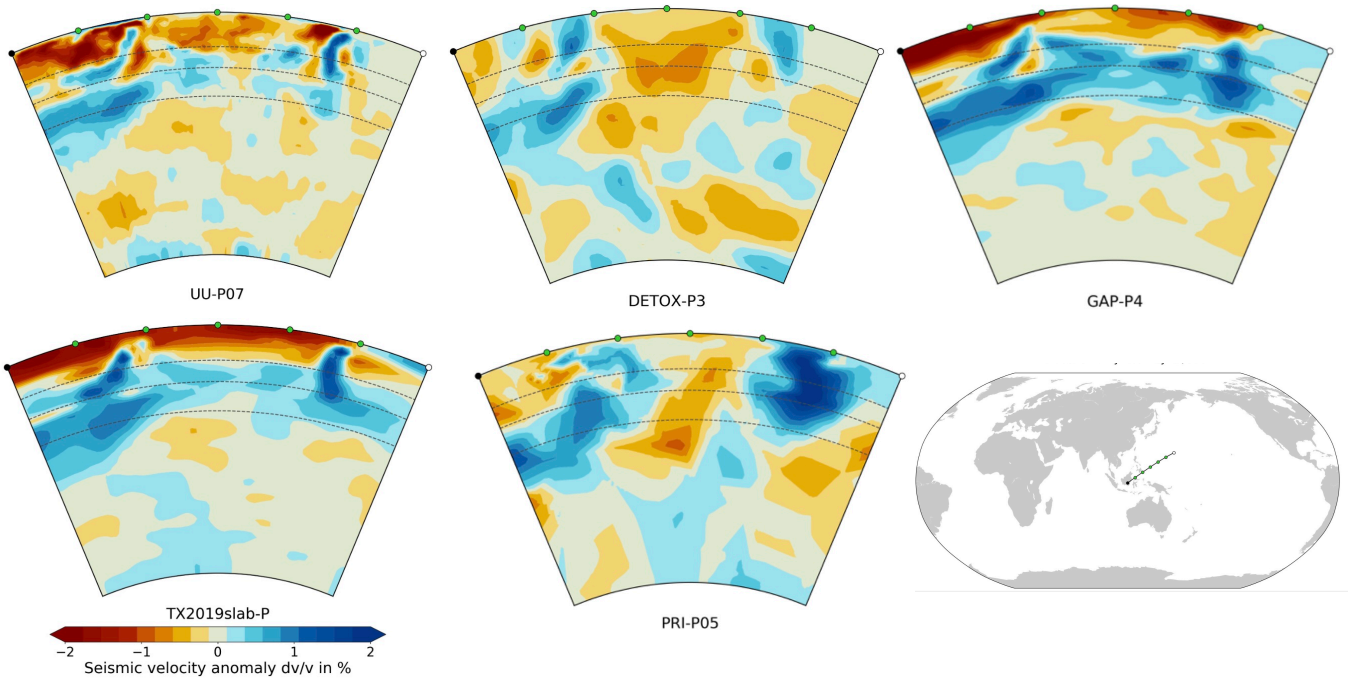

Figure 1 Comparison of different global P-velocity models across a depth section from 1.7S, 114.6E to 20.9N, 154.8E, which incorporates the subduction zones near the Philippines and the Mariana Islands. The broken lines indicate 410, 660 and 1000 km depth levels. The plots extend to the core-mantle boundary (CMB). The images were produced with SubMachine (Hosseini et al., 2018).

for subduction zone imaging, but it is representative for much of the rest of the globe. Oceanic areas in particular suffer from a lack of ray coverage, which even full waveform inversions (FWI) do not solve (Wamba et al., 2025).

Ray coverage depends strongly on the data set used. The resolution that can be obtained can also be limited by the scale of the parameterization used. Some tomographic models, notably those based on a spherical harmonics parameterization, do not attempt to obtain a maximum resolution where data density is high, but instead accept a less-than-optimal data fit in exchange for a more uniform resolution across the globe (Boschi and Dziewonski, 1999). Zhou et al. (2024) report an improvement of up to 44% in data fit when such models are fused with high-resolution models.

In this paper we combine several very large data sets, including some that have not been used before. The prime motivation for our inversion comes from the recent project SPPIM – South Pacific Plume Imaging and Modelling (Simon et al., 2020, 2022) – which involved the launching of 49 floating seismometers or 'MERMAIDs'[1] (Simons et al., 2006, 2009; Hello et al., 2011; Hello and Nolet, 2020) that have been transmitting seismograms from the South Pacific since mid-2018. When inverting the data for this experiment, we must avoid that delays that are acquired by velocity anomalies outside of the South Pacific wrongly influence the regional tomographic images. We must therefore resolve those anomalies as well, and we do this by embedding them in a global inversion, using arrivals from seismic waves that cover the full volume of the mantle. This paper describes the data and inversion procedure in detail, and presents the new global model. It is intended to serve as the reference for future work that will discuss the resulting velocity anomalies found in the South Pacific mantle, the Tonga-Kermadec subduction zone – both of which benefit from the addition of MERMAID data – as well as the global pattern of subduction. In addition to the new MERMAID data we also added cross-correlation delays from the European Research Council (ERC) project 'Globalseis', in particular a large set of PP delays, which have not yet been used in a global inversion.

[1] MERMAID: Mobile Earthquake Recording in Marine Areas by Independent Divers

2 Data sources

In the tomographic inversion we used both picked arrival times and delay times obtained by cross-correlation. The bulk of the arrival times comes from the ISC-EHB database (see Tab. 1). However, we have supplemented this with data from temporary networks at sea, including floating seismometer MERMAID networks, which provide raypath coverage that is absent from the ISC-EHB set, and by finite-frequency data that have a volume sensitivity extending beyond the ray-theoretical sensitivity of the ISC-EHB delays. In all cases, we eliminated any suspected misprints or other errors in the data by rejecting a priori any travel-time anomalies in excess of 10 s. We describe the data sources in this section and identify the acronyms by which each of them is referred to in Tab. 1 and 2. In these tables N_{delays} refers to the number of data, Δt_{av} and 'std.' are average and standard deviation σ of the data set as observed, and σ_{av} is the average of the estimated standard errors (all before outlier removal). The

column labelled 'outl.' gives the fraction of outliers: after a first inversion attempt with only minimal damping, any delay that could not be fitted within 3σ was rejected as 'outlier'. For the cross-correlated delays we also list the number of paths and events.

Though the data come with a formal or estimated standard error, these may be optimistic since they do not take systematic errors into account, e.g., due to a wrongly estimated source time function or neglect of effects of attenuation when cross-correlating, or bathymetry errors for the MERMAID data. We therefore imposed a minimum standard error of 0.6 s, which is close to the average of empirically determined teleseismic P-delay errors in the EHB set as shown in Table 3 of Nolet and van der Lee (2022).

2.1 ISC-EHB (acronym: EHB)

The bulk of the picked arrival times comes from the precious and massive data collected by the International Seismological Data Center in the U.K., which go as far back as 1964. A subset of high-quality misfits (or 'delays') of these data after hypocentre determination is known as the 'ISC-EHB' data set (Engdahl et al., 1998, 2020). Recently, Nolet (2023) processed this database to derive more than 12 million well-distributed 'path-averaged' delay times for P and S phases with respect to the spherically symmetric model AK135 (Kennett et al., 1995). These are the data that are used in this study. We prefer to use path average delays because (1) it renders the inversion problem more manageable than with the more than 100 million delays in the original ISC data set, and (2) it spreads the information more evenly over the globe (see next section). Standard errors were derived from the statistics of the delays in each averaged bundle. If only one ray is present in a bundle, standard errors were taken from Nolet and van der Lee (2022). Table 1 lists the number of P, Pn, pP and PKP (ab and bc branch) delays used. The pP data require special treatment, because the ISC-EHB delays are for a reflection at the ocean bottom when the bathymetry is deeper than 1500 m (Engdahl, pers. comm., 2025), but otherwise with respect to the surface of the solid Earth. We refrained from using the PP delays, because this is an emergent minimax arrival of which the onset is not only difficult to pick, but for which a linearized ray-theoretical interpretation is questionable, since a (deflected) first arrival may be scattered from a location far from the unperturbed ray.

Source	type	N_{delays}	outl. (%)	Δt_{av} (s)	std. (s)	σ_{av} (s)
EHB	P	7 310 218	0.6	0.22	1.06	0.75
EHB	Pn	948 207	4.3	0.16	2.12	0.94
EHB	pP	425 413	1.8	0.43	2.15	1.35
EHB	PKPab	153 364	1.0	0.31	1.22	0.89
EHB	PKPbc	261 208	0.4	0.26	0.97	0.65
JMS	P	4 072	1.8	0.31	1.72	0.70
GAL	P	4 286	5.3	1.17	2.14	0.61
GAL	pP	172	6.4	4.23	2.68	0.60
GAL	PKP	760	0.8	0.42	1.52	0.61
SPM	P	39 922	0.8	0.62	2.05	0.71
DTX	Pdif	47 639	0.8	-0.52	2.48	0.61

Table 1 Statistics of the picked arrival times before outlier removal.

2.2 JAMSTEC OBS and Polynesian OBS network data (JMS)

To further aid the study of the Pacific superplume structure targeted by SPPIM, we added local OBS data. This data set comprises not only 9 OBS in Polynesia, but also 11 OBS in the Northwest Pacific, as well as GSN station H2O east of Hawaii. The Polynesian BBOBS network operated from 2003 to 2005 (Suetsugu et al., 2005) and its data were earlier used by Obayashi et al. (2016) for a tomographic interpretation of the upwelling in the South Pacific. Added to this were data from other GSN stations, to enable event corrections during the inversion. We used P arrival time picks only, from a total of 251 events. In the absence of information on the standard errors, we assigned errors of 0.7 s to them, based on our own experience of picking OBS and island GSN data.

2.3 Galápagos MERMAID data (GAL)

Between May 2014 and October 2016, a set of nine floating seismographs known as MERMAIDs (Simons et al., 2009) operated near the Galápagos islands (Nolet et al., 2019). MERMAIDs normally float at 1500 m depth and come to the surface to transmit seismic signals picked up by the hydrophone. The recording location is interpolated from GPS locations at each surfacing. Nolet et al. (2024) have shown that the equivalent timing error due to instrument mislocation is generally well below 0.1 s and negligible for tomographic purposes. We used the 580 arrival times picked from the MERMAID seismograms, augmented with local island and GSN data to allow for corrections of the 256 events recorded. Standard errors were individually estimated for each pick.

2.4 South Pacific MERMAID data (SPM)

A network of 49 MERMAIDs (South Pacific Plume Imaging and Modeling, or SPPIM) was launched using floats from SUSTech, Princeton, JAMSTEC/Kobe University and Geoazur between June 2018 and September 2019. Here we use a set of data from the network obtained until November 2023. Though a handful of the 49 instruments were still actively transmitting beyond their designed life expectancy of five years, project SPPIM is approaching its end at the time of submission of this paper. We used 4954 picked P arrivals from 1927 events, and added picks from ISC (until 2020) or NEIC (after 2020) from nearby stations to enable event corrections when inverting the travel-times. Because we suspect that pP arrivals from very shallow events can easily be misidentified as P, we did not use the picks from 1237 events with depth < 20 km which can be more accurately interpreted using the waveform fitting method of Pipatprathanporn and Simons (2024). See Nolet et al. (2025) for station locations (Figs. 1 and 3) and more details on the picking of arrival times and the determination of standard errors.

Source	type	N_{delays}	N_{paths}	N_{events}	outl. (%)	Δt_{av} (s)	std. (s)	σ_{av} (s)
DTX	P	1 350 276	234 154	1426	0.6	-0.83	2.13	0.60
GLS	P	23 432	6 504	59	3.1	-0.15	1.11	0.69
GLS	PP	94 680	40 621	248	1.9	1.93	1.94	1.84
GLS	pP	16 380	4 290	39	3.3	-0.26	2.65	0.61
GLS	PKP	935	231	15	0.5	-0.58	0.93	0.77
GLS	PcP	106	46	3	12.3	-0.36	1.57	0.87

Table 2 Statistics of delays determined by band-filtered cross-correlation, before outlier removal.

2.5 Cross-correlation delays of P and Pdiff (DTX)

Hosseini et al. (2020) derived the P-wave model DETOX-P3 from delays using the cross-correlation method of Sigloch and Nolet (2006) modified by Hosseini and Sigloch (2015), for up to eight period bands between 30 and 3.7 s. The extra information they provide comes from the dispersion of the frequency-dependent delays. After EHB, this is our largest subset of data but, like EHB, the paths are dominated by those to stations on the continents. Because of some issues with lost or uncertain metadata information for earlier events, we used only those from 2008 onwards. Delays with a correlation coefficient below 0.90 were rejected, as were data for which fewer than 4 bands could be correlated. The correlation algorithm provided formal standard errors, which were generally ≤ 0.4 s, below our imposed 0.6 s minimum. To compute the finite-frequency sensitivity, which depends on the filtered spectrum of the P-wave, Hosseini assumed a locally flat P-wave spectrum, so that only the filter response determines the sensitivity. Also in this data set is a large set of P diffracted arrivals. Since the software we use for finite-frequency delays computes the sensitivity using dynamic ray-tracing (Dahlen et al., 2000; Tian et al., 2007a,b), we cannot handle diffracted arrivals this way. Instead, we have fitted a straight line to the delay as a function of period and sampled this linear function at a period of 0 s to derive an approximate 'picked high frequency' delay for Pdiff, rejecting those delays for which the standard error (calculated from the statistics of the linear fit) exceeded 0.9 s. Fig. S22 shows some examples. These have been interpreted with ray theory.

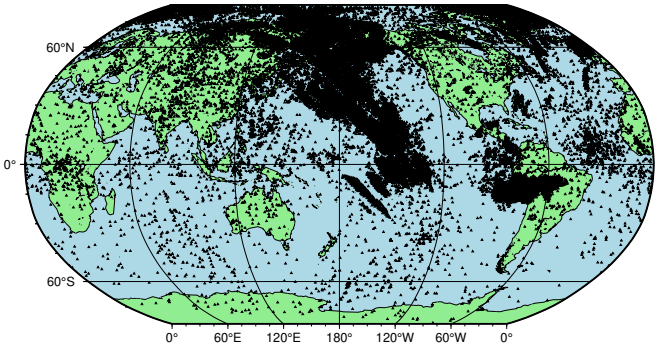

Figure 2 Reflection points of 94 680 PP-waves used in this study.

2.6 Cross-correlation delays of P, PP, pP, PcP and PKP (GLS)

As part of the ERC project 'Globalseis' we measured delays for all five phases from a well-distributed set of 157 events, using the method described by Bonnin et al. (2014), which differs from that used for DTX: instead of correlating with a synthetic, each seismogram for an event is correlated with all others in a series of frequency bands. Individual delays are determined by solving a system of equations that is overdetermined except for one constant time factor – which is chosen such that the delays fit best to AK135 (the origin time correction in the inversion may correct this choice, if necessary). We use the overlapping Gaussian filters described by Hung et al. (2000), starting with one centered at 0.031 Hz (period T=32 s), and halving the period until T=2 s, rejecting correlation coefficients below 0.9. Rather than assuming a flat spectrum, we estimate the spectrum of the P-wave for each event to compute the finite-frequency sensitivity. 50% of the acceptable data reach a dominant frequency of the P-wave > 0.07 Hz, for 20% the dominant frequency exceeds 0.20 Hz. To these 157 events we added PP data from another 144 events in an effort to better cover the oceanic areas. We used data from the Global Seismic Network downloaded from the IRIS data management centre (now EarthScope) for events between 2000 and 2013. The location of the PP reflection points is shown in Fig. 2. Note that the sensitivity near the reflection point is spread out because of finite-frequency effects. For example, for a dominant period of 20 s and an epicentral distance of $60°$, the reflection 'point' is in reality a volume with a size of about 400 km at the surface, and sensitivity extending to 300 km depth (Hung et al., 2000).

3 Tomographic inversion

We assume a relationship between the delays and the model that is sufficiently linear so that the inverse problem can be solved with an iterative linear solver and avoids tedious 3D raytracing after each iteration. Bijwaard and Spakman (2000) show that nonlinearity affects the amplitude of ray-theoretical inversions but leaves the shape of anomalies relatively undistorted; Mercerat and Nolet (2013) confirmed linearity of cross-correlation delays interpreted with finite-frequency kernels as long as velocity anomalies are below about 10% (which they are in this study).

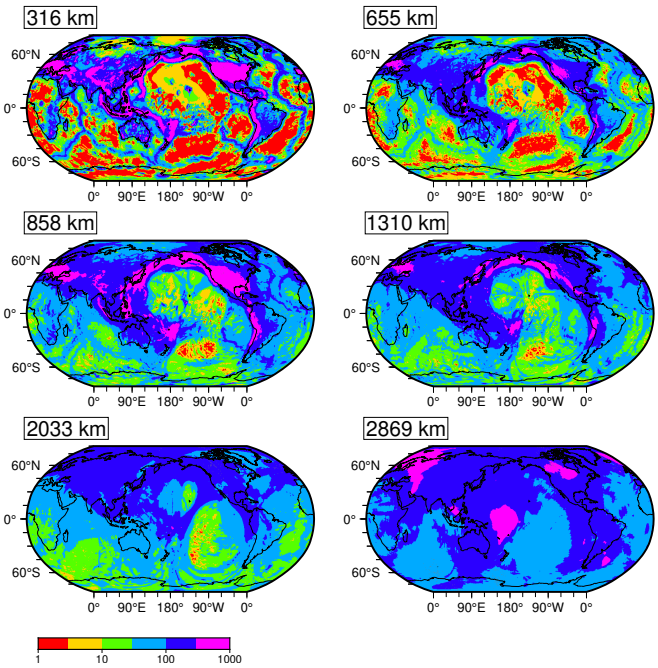

Figure 3 Column density of the system (1) at six representative depths in the mantle. The colour scale is logarithmic.

3.1 Parameterization

We parameterize the Earth in voxels, each with a P-velocity anomaly. To avoid that a coarse parameterization might needlessly limit the resolution and worsen the data fit, we deliberately overparameterize. We use the cubed Earth parameterization of Charléty et al. (2013), which divides the Earth's mantle into six cubes. Each cube is parameterized horizontally by 128×128 voxels, and vertically by 37 layers. The average voxel size varies from 78×78 km at the surface to 43×43 km near the core-mantle boundary (CMB). The height of each voxel is 90.4 km except in the crust (two layers of 22.6 km) as well as near upper mantle discontinuities and D" (layer thicknesses 45.2 km). This yields 3 637 248 velocity parameters. To this are added corrections to the origin time, latitude, longitude and depth of each of the 25 399 events. The total number of unknowns is therefore 3 738 844. Even though the number of data (10 571 152) is much larger, the system is not overdetermined since the data coverage is very unequal, with an abundance of ray paths under the continents in the northern hemisphere and scant coverage elsewhere (Fig. 3).

The linearized relationship between the data vector $\mathbf{d}$ and the model parameter vector $\mathbf{m}$ is:

$$\mathbf{A}\mathbf{m} = \mathbf{d}\,, \tag{1}$$

where the matrix $\mathbf{A}$ contains both ray-theoretical and finite-frequency kernels that describe the sensitivity of delays to the P-velocity perturbations and source corrections in $\mathbf{m}$. The system (1) is scaled and rendered dimensionless such that the standard error of each delay d_i is 1, and the parameters m_i are scaled to unit variance by dividing them by their prior uncertainty: 1% for P-velocity anomalies, 1 s for event origin time and 20 km for hypocentre depth, longitude and latitude (Nolet, 2008).

3.2 Forward modelling

For the forward modelling, we compute ray trajectories and invert with ray theory for onset time picks (Tab. 1). Cross-correlated delays (Tab. 2) are inverted using finite-frequency kernels (Dahlen et al., 2000; Nolet, 2008). To compute predicted travel times, we adopt a mixed 1D/3D background model with the radially symmetric P-velocity Earth model AK135 below the crust, and the top of LITHO1.0 (Pasyanos et al., 2014) in the crust. For OBS and MERMAID data we replace the LITHO1.0 ocean depth with the bathymetry of GEBCO2014 (Weatherall et al., 2015) at their location. Since the reflection coefficient at the ocean bottom is about 0.8-0.9 (depending on slowness), we used this interface as reflector when computing the predicted arrival times. The 3D background crustal model avoids unwanted effects of damping in the inversion (next section). For example, we do not wish to push the solution towards the continental AK135 model where there is an ocean.

3.3 Preconditioning and regularization

Since at least part of the model is underdetermined, we must regularize the solution in some way.

We first note that, if we add smoothness regularization to the system (1), its convergence in iterative solvers can be sped up using preconditioning, substituting $\mathbf{m} = \mathbf{B}\mathbf{y}$ where $\mathbf{B}$ approximates the inverse of the Laplacian ∇^2 (VanDecar and Snieder, 1994): it is a matrix that attempts to smooth $\mathbf{y}$. We designed $\mathbf{B}$ such that it replaces every model parameter m_i by the average of its neighbours, after copying $\mathbf{y} = \mathbf{m}$:

$$m_i = \frac{1}{\mathcal{N}_i} \sum_{j \in \mathcal{N}_i} y_j\,, \tag{2}$$

where $\mathcal{N}_i$ denotes the number of neighbours of voxel i, which is 6, or 5 at the top and bottom of the model (we do not include diagonal neighbours). Note that $\nabla^2\mathbf{m} = 0$ if the result of the multiplication were to be such that every new m_i is indeed the average of its neighbours – which normally it is not since those neighbouring voxels are updated as well. But if repeated many times (which is the case if the linear equations are solved iteratively) it will nudge the model to one that satisfies Laplace's equation. For the part of $\mathbf{m}$ that includes source corrections, the corresponding columns of $\mathbf{B}$ are simply a unit matrix since no averaging should be done over corrections.

We combine the preconditioning with two regularizations. In the first one we damp the voxels to zero by imposing $\epsilon_1 D_{ii} m_i = 0$, where the D_{ii} are elements of a diagonal matrix $\mathbf{D}$. We choose them proportional to the Euclidean column density:

$$D_{ii} = \sqrt{\sum_j A_{ij}^2} + \epsilon_w\,, \tag{3}$$

with addition of a water level ϵ_w equal to 10^{-4} times the largest column density. We only scale the damping parameter and apply no explicit column scaling. Fig. 3 shows the column density, a proxy for ray coverage, in the mantle using a logarithmic scale. As a rule of thumb, the upper mantle column density differs by more than an order of magnitude between the ill-served southern hemisphere and continents in the northern hemisphere. The lower mantle has significantly fewer 'ray deserts' (red colours) than the upper mantle. The most equitable column density is found in the deepest layer, which benefits from the DTX diffracted P-waves at the CMB. Comparison with Fig. 2 shows that the central part of the North Pacific upper mantle is adequately filled in with PP ray paths reflecting there, which suggest that inclusion of cross-correlation of PPP arrivals in future inversions might significantly enhance the coverage both East and West of the area where PP reflections are abundant.

The second regularization imposes $\epsilon_2 \nabla^2 \mathbf{m} = 0$, i.e. it penalizes roughness. We use a first-order finite-difference approximation for the second derivatives in the three spatial dimensions. Putting all this together, we solve the combined system of $N \times M$ equations first for $\mathbf{y}$:

$$\tilde{\mathbf{A}}\mathbf{y} = \begin{pmatrix} \mathbf{AB} \\ \epsilon_1 \mathbf{D} \\ \epsilon_2 \nabla^2 \end{pmatrix} \mathbf{y} = \begin{pmatrix} \mathbf{d} \\ \mathbf{0} \\ \mathbf{0} \end{pmatrix} , \tag{4}$$

after which we recover $\mathbf{m} = \mathbf{By}$. To solve (4) we use the iterative solver LSQR (Paige and Saunders, 1982; Nolet, 1985) which we adapted for parallel processing. We output intermediate results for $\mathbf{y}$ every 500 iterations, which enables us to monitor progress during time-consuming inversion runs.

We use two measures for the convergence of (4): the (reduced) χ^2 for the (univariant) data is defined as:

$$\chi^2_{\mathrm{d}} = \frac{1}{N_d} \sum_{i=1}^{N_d} [d_i - \sum_j A_{ij} m_j]^2 , \tag{5}$$

with N_d the number of data. Thus, we strive for the (dimensionless) $\chi^2_{\mathrm{d}} \approx 1$ so that, on average, the data are fitted no better or worse than their assigned standard error. The less than 5000 picks from the MERMAID data are dwarfed by the almost half a million picks from EHB in the same area. Upweighting important data to compensate for their scarcity is an effective policy in inversions, e.g. Takeuchi and Kobayashi (2004), though it may also amplify the effect of errors. To speed up their convergence in LSQR we have given the SPM data extra weight by multiplying their contribution to χ^2_{d} in (5) by a factor of 16 – which we found to be sufficient after experimenting with larger values. As will be shown in section 4, there is no noticeable effect of error amplification with this factor.

The total fit – including the fit to the regularization equations in (4) – is found by summing over all N equations in (4):

$$\chi^2_{\mathrm{tot}} = \frac{1}{N} \sum_{i=1}^{N} [d_i - \sum_j \tilde{A}_{ij} y_j]^2 , \tag{6}$$

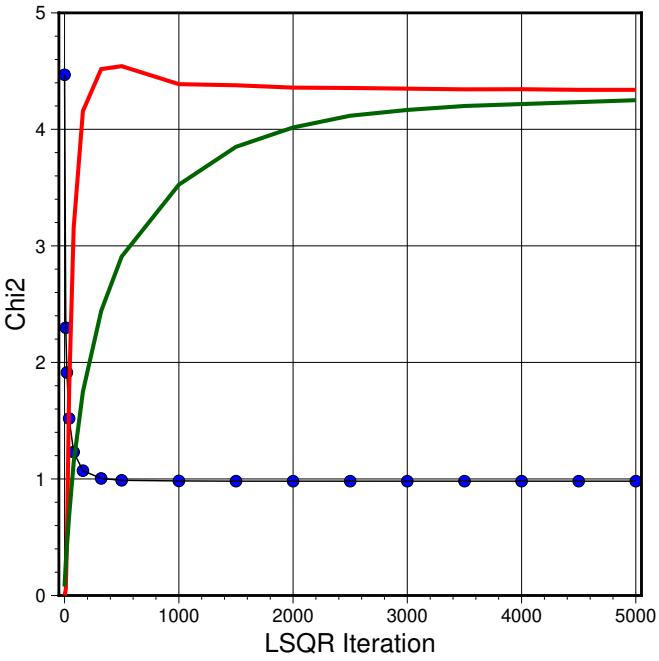

Figure 4 Convergence of the tomographic solution. The connected blue dots give the convergence of the data showing χ^2_{d} (eq. 5) approaching 1; the red line gives the misfit to the regularization equations ($\chi^2_{\mathrm{tot}} - \chi^2_{\mathrm{d}}$), and the green line the Euclidean norm of the solution $|\mathbf{m}|^2$ (both arbitrarily scaled such as to show their convergence).

3.4 Inversion

We inverted the data keeping $\epsilon_2/\epsilon_1 = 2$ constant while searching for an acceptable level of regularization – with some trial and error we arrived at the preferred solution with a misfit $\chi^2_d = 0.98$. If we increase ϵ_2/ϵ_1 and put more emphasis on smoothing, we find that subduction zones, which are generally well resolved, are less sharply imaged. On the other hand, if we lower the ratio too much and give prominence to damping, artefacts caused by the variations in ray density dominate. As we shall see later in resolution tests (e.g. Fig. S21), the damping leads only to minor loss of amplitude for much of the lower mantle. Though the fit to the data converges after about 1000 iterations, the final Euclidean norm $|\mathbf{m}|^2$ of the model is not reached until we have done about 5000 iterations (Fig. 4) when the smoothing by relaxation seems to have converged.

The preferred solution is shown in Fig. 5 and named UNICA25 following a tradition to name the model after its native institution – Université Côte d'Azur – and its year of birth). Tab. 3 lists the misfit for each data set separately. The table also lists the average absolute misfit $|\Delta t|_{\mathrm{av}}$ in seconds, as well as the average of the signed misfits Δt_{av}. Not surprisingly, first arrivals P and PKP fit better than later arrivals, but most sets have a misfit that is individually acceptable, with the exception of the Galápagos data and a surprisingly large misfit for EHB-Pn; contrary to what its name suggests, this Pn is not just the Moho headwave, but includes diving waves bottoming above the 400 km discontinuity. We suspect some ISC data to be affected by the triplications that complicate the identification of this wave. The average mis-

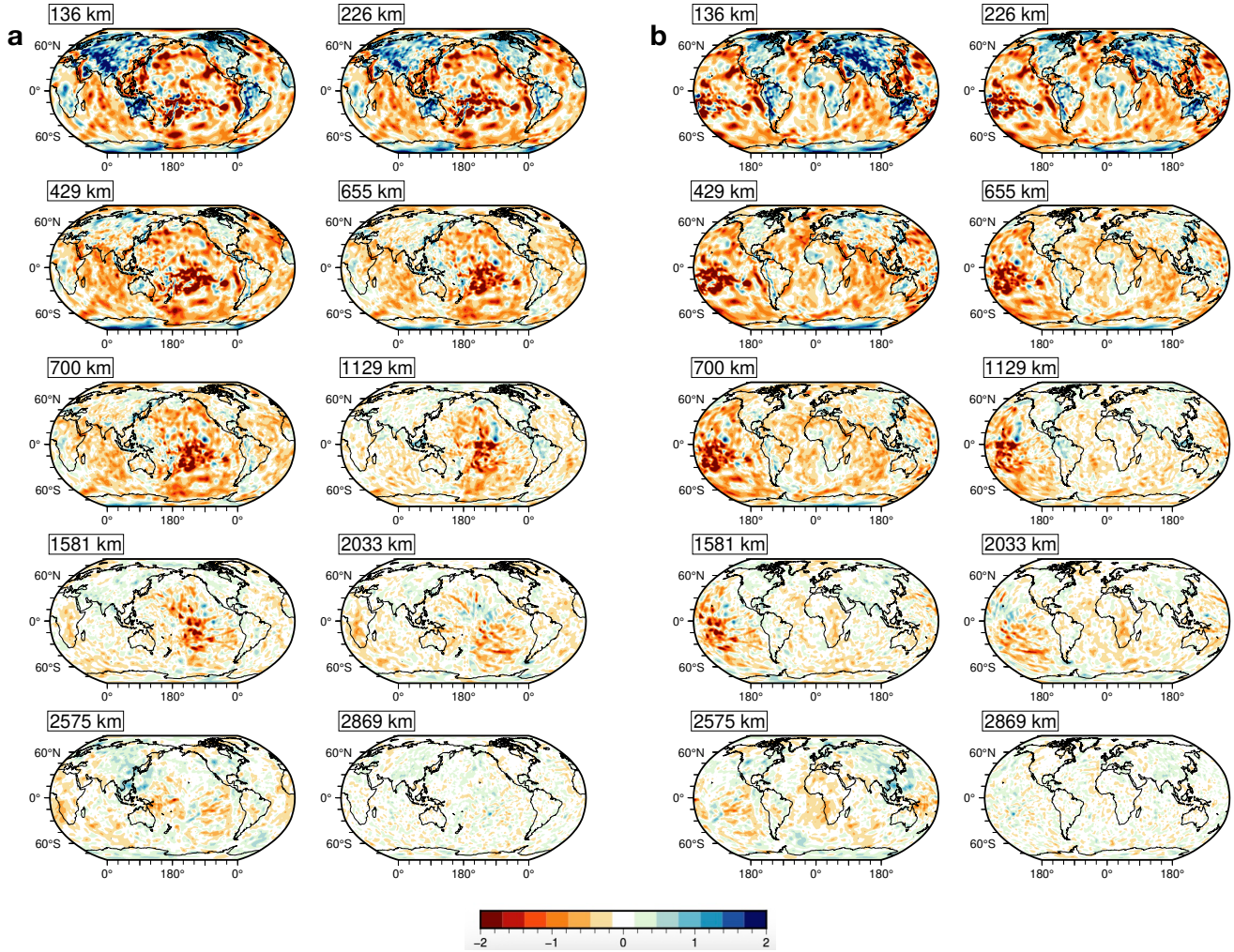

Figure 5 The preferred tomographic solution UNICA25 plotted at ten depths, centred at $180°$E (a) and $0°$E (b). The colour scale is in per cent with respect to the background model (AK135 at mantle depths). See Figs. S1-S20 in the Supplement for blown-up versions at each depth with scale adapted.

fit $\Delta t_{\rm av}$ is within 0.2 s of zero, with one exception (GLS-PKP, which is a very small data set).

Fig. 6 shows the maximum and minimum anomaly as a function of depth, as well as the average and root-mean-square (RMS) value. But, since the effect of regularization differs geographically, the global RMS is not a very useful measure of model heterogeneity since, in the upper mantle beneath the oceans, the model is strongly biased towards zero (see next section).

The global average of velocity anomalies (RMS) is 0.49%. The velocity anomalies vary between -6.18 and +4.48% with the largest negative anomaly at a depth of 135 km in SW Polynesia ($30.9°$S, $178.4°$E). The average anomaly over the whole model is slightly negative (-0.11%) as expected since most of the observed delays have are slightly positive average $\Delta t_{\rm av}$ with respect to the background model AK135 + LITHO1.0 crust. The RMS change in the source corrections is $0.60\sigma_{\rm prior}$, i.e. 12 km for hypocentral coordinates and 0.6 s for the origin time.

4 Resolution tests

We tested the resolution of the data by generating synthetic data for a regular distribution of anomalies with a 3D Gaussian velocity profile. The maximum anomaly was set at $\pm 4\%$, which is of the order of the largest anomalies found in the upper mantle (Fig. 6c). The anomalies are generally spherical, with the $1/e$ radius R_e defining their scale. We placed anomalies at six depth levels, regularly spaced and fluctuating between positive and negative velocity values. Fig. 7 shows the resolution at a length scale of about 300 km ($R_e = 150$ km), Fig. 8 at 500 km scale ($R_e = 250$ km). For the larger shallow ones, we reduced the depth extent to avoid overlap: at 136 km depth the depth extent was not allowed to go beyond ± 200 km ($1/e$ level), and similarly ± 300 km for the spheres centred at 655 km. If the R_e exceeds this for the vertical size, the anomaly is therefore an ellipsoid rather than a sphere.

The plotting in Figs. 7 and 8 is done at ± 1 and $\pm 2\%$ colour scale, respectively, rather than using the input extremes of 4%, to bring forward the more weakly resolved parts of the globe.

The lack of resolution beneath the oceans is still severe in the upper mantle, except east of Tonga-Fiji

		UNICA25			GLAD-M35			REVEAL		
Data	N	χ^2_{d}	$\lvert\Delta t\rvert_{\mathrm{av}}$ (s)	Δt_{av} (s)	χ^2_{d}	$\lvert\Delta t\rvert_{\mathrm{av}}$ (s)	Δt_{av} (s)	χ^2_{d}	$\lvert\Delta t\rvert_{\mathrm{av}}$ (s)	Δt_{av} (s)
EHB P	7264150	0.8	0.7	0.01	2.4	1.1	-0.02	1.7	1.0	-0.05
EHB Pn	906913	2.4	1.4	0.01	9.9	2.7	0.98	12.3	2.9	-0.56
EHB pP	417520	1.1	1.4	0.16	2.9	2.3	-0.57	2.8	2.2	1.02
EHB PKPab	151751	1.2	1.0	0.03	5.1	1.9	-0.57	6.6	2.1	1.35
EHB PKPbc	260072	1.1	0.7	0.01	8.2	1.8	-1.01	7.9	1.8	1.18
JMS P	3999	1.3	0.8	-0.00	2.3	1.1	0.02	3.4	1.3	-0.01
GAL P	4059	2.4	0.9	0.01	5.8	1.5	0.06	5.6	1.4	-0.03
GAL pP	161	2.7	1.0	0.05	5.3	1.4	0.04	5.1	1.4	0.02
GAL PKP	754	2.8	1.0	-0.02	9.3	1.8	-0.06	8.5	1.8	-0.00
SPM P	39599	1.6	0.9	-0.03	5.3	1.6	-0.06	5.0	1.6	-0.08
DTX Pdif	47242	1.3	0.7	-0.18	4.1	1.2	-0.66	2.0	0.9	-0.08
DTX P	1342462	0.8	0.5	0.01	1.9	0.8	0.02	1.4	0.7	0.00
GLS P	22700	1.2	0.8	-0.05	2.1	1.0	-0.07	1.6	0.9	0.03
GLS PP	92917	0.5	0.9	-0.01	1.0	1.2	0.04	0.8	1.0	0.01
GLS pP	15840	1.2	0.7	-0.00	2.4	0.9	-0.00	1.9	0.9	0.01
GLS PKP	921	1.2	0.8	-0.32	5.3	1.6	-1.31	1.6	0.9	-0.45
GLS PcP	93	1.4	1.0	-0.30	4.1	1.6	0.21	1.4	1.0	-0.27

Table 3 Misfit χ^2_d, average absolute misfit $|\Delta t|_{\mathrm{av}}$ and average misfit Δt for UNICA25, GLAD-M35 and REVEAL.

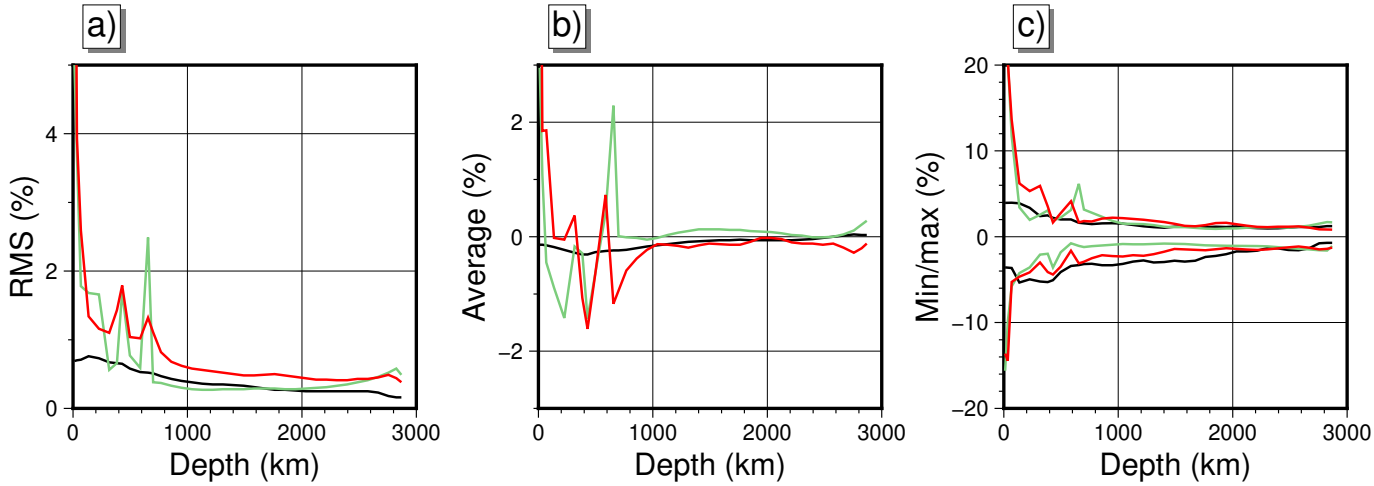

Figure 6 From left to right: (a) the RMS deviation for ΔV_P at each depth, (b) the average, and (c) extreme values across the model, for model UNICA25 (black), GLAD-M35 (green) and REVEAL (red). Anomalies are with respect to AK135 in the mantle, and with respect to LITHO1.0 in the crust. The peaks in the RMS and the average anomaly for the FWI models near the 410- and 660-km discontinuities are discussed in section 5.

where the MERMAIDs show their influence, but improves markedly in the lower mantle. At 1400 km the anomaly shapes are resolved almost everywhere at the 500 km scale ($R_e = 250$ km), except for a small area in the South Pacific near 90°W, 60°S, and north of 30°S the resolution is also good for $R_e = 150$ km. At the very deepest level the shapes are smeared by preferred directions of the ray trajectories that reach that deep, but at shallower levels there are few signs of such smearing.

To estimate the influence of data errors, we also inverted a data vector of pure noise with the same statistical properties as the estimated standard errors. The result of that is shown in Fig. 9. Note that this cannot be interpreted as a final error estimate for the values in UNICA25, since the inverted amplitudes are also affected by damping due to lack of full resolution. For the best resolved areas, the resolution tests show a slight loss of amplitude, with an output near 3.5% for an input of 4% at 500 km scales (Fig. S21). It is noteworthy that UNICA25 at the deepest level near the CMB has velocity amplitudes mostly below the 95% confidence level, either reflecting a very much reduced sensitivity to temperature, or an amplitude affected by composition and temperature variations that influence V_P in different directions. What one sees at this depth is therefore largely noise.

Fig. 10 shows the solution we obtain in the same cross-section as Fig. 1. In the upper mantle transition zone, where the models differ strongly, UNICA25 agrees with DETOX and PRI-P05 that the transition zone has low velocities in the central part of the section.

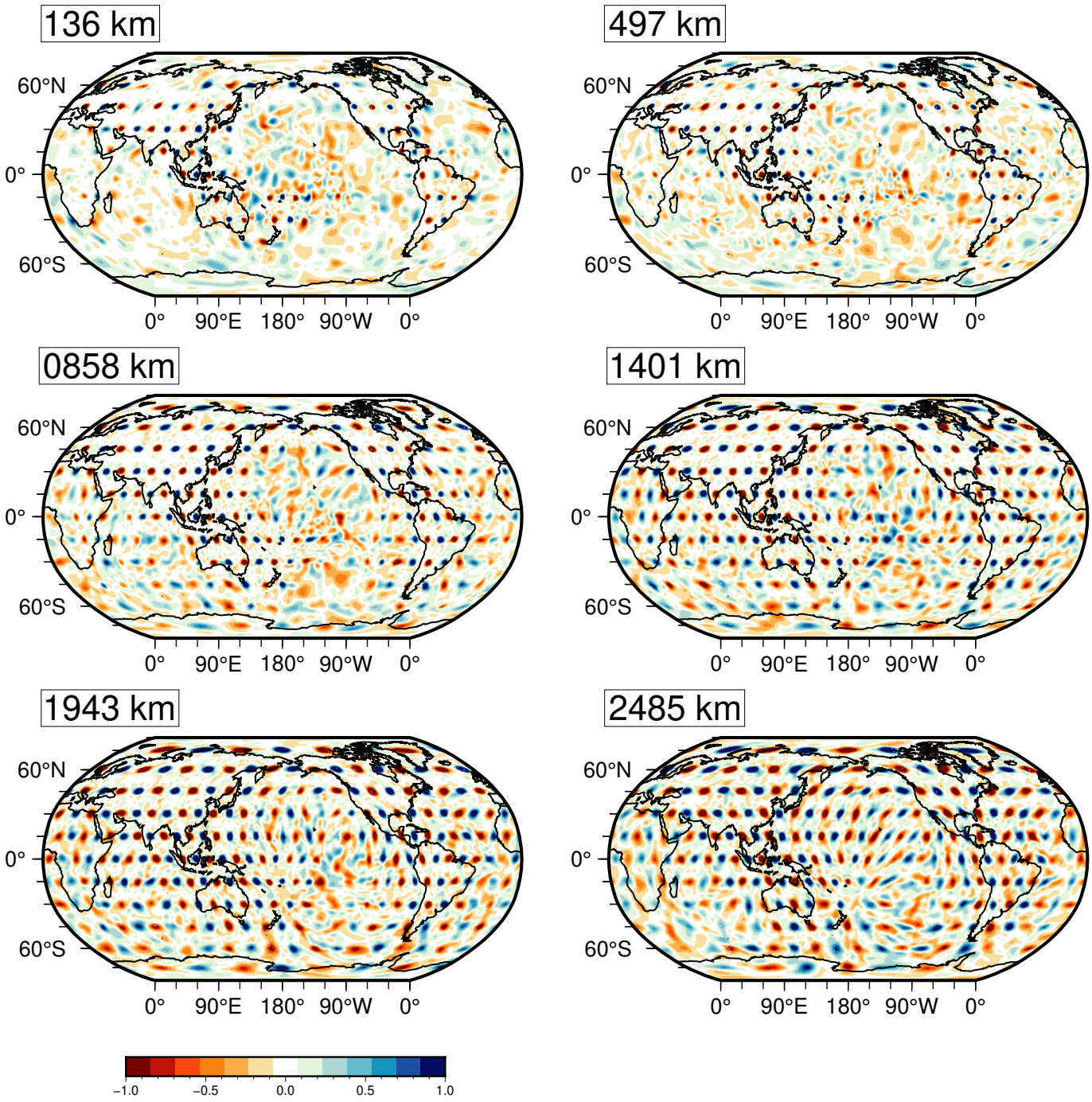

Figure 7 Result of the 300 km resolution test for Gaussian anomalies of radius R_e =150 km and maximum anomaly 4%.

5 Comparison with Full Waveform Inversion

In Figs. S23 and S24 we compare model UNICA25 with several older global P wave models. We have also contributed the model to Submachine (Hosseini et al., 2018) so that readers can create their own maps or cross-sections. Except for anomalies near subduction zones and stations, the large negative anomalies in oceanic areas are absent in these older models, even in the lower mantle, where the resolution tests show that UNICA25 is reliably reproducing synthetic anomalies. The fact that anomalies in the less-well resolved parts of the upper mantle are not damped away in our model by regularization indicates that some negative anomalies are probably strong and large enough to influence the inversion result. We notice that recent local inversions also show negative upper mantle P anomalies in excess of -3% (Kang et al., 2023; Eilon et al., 2022). We suspect that the increase in resolution is mostly due to the volume sensitive finite-frequency data, especially the large GLS-PP data set in the upper mantle, though it is likely that the dramatic increase of the EHB data volume in recent years has also contributed to the oceanic lower mantle amplitudes. Our prime focus in this section is therefore on a comparison with two very recent models obtained with Full Waveform Inversion, which is also volume-sensitive and widely considered the state-of-the-art in seismic tomography today.

With the exception of DETOX-P3 (Hosseini et al.,

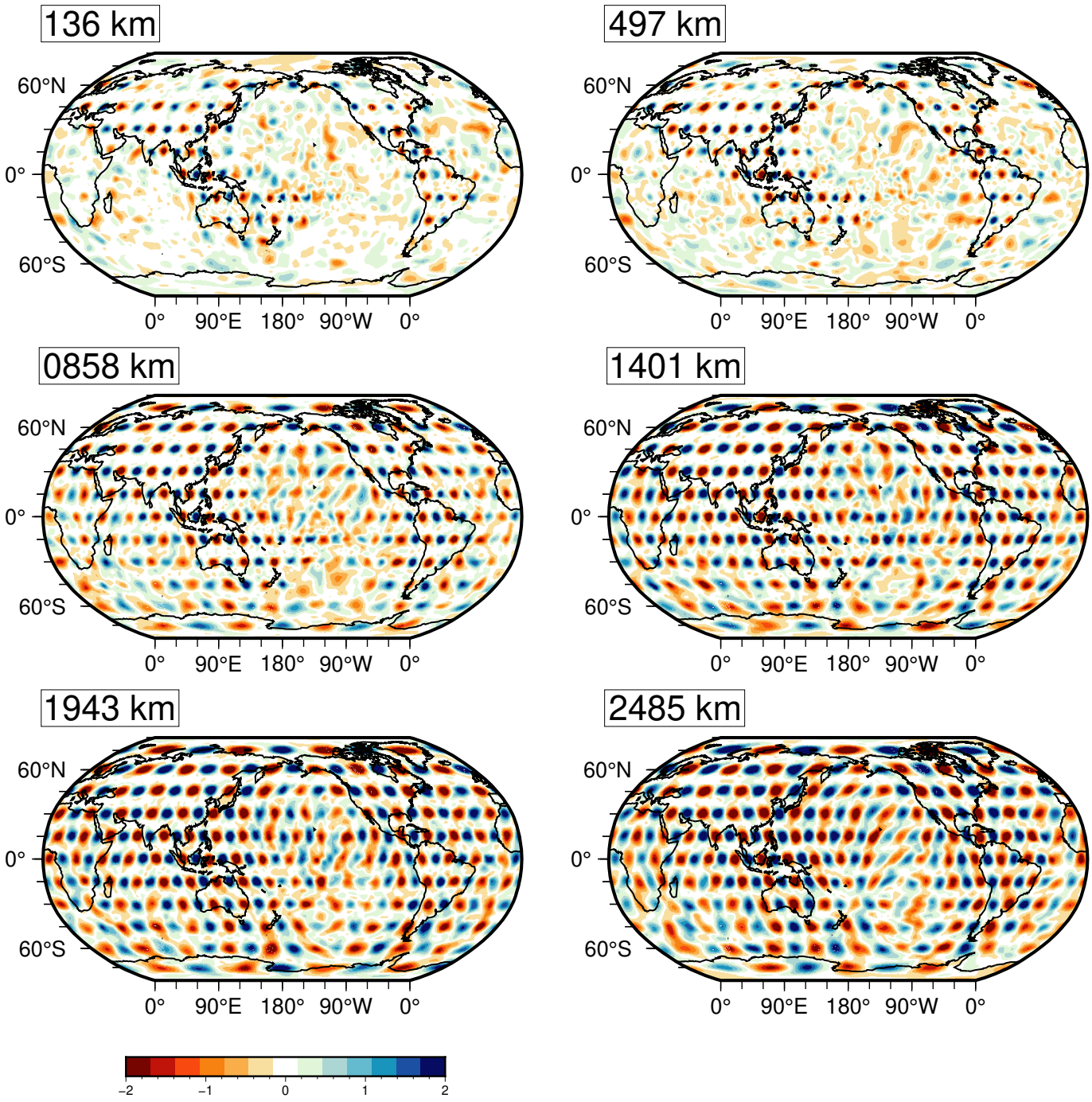

Figure 8 Result of the 500 km resolution test for Gaussian anomalies of radius R_e =250 km and maximum anomaly 4%.

2020), the most recent high-resolution global models for V_P are the result of a combined inversion of P, S and surface waves for a model that includes anisotropy. Model SPiRaL (Simmons et al., 2021) used about 4 million P and S arrivals and almost 2 million surface wave dispersion data to invert for a model with more than 10 million parameters that includes radial anisotropy. Models GLAD-M35 (Cui et al., 2024) and REVEAL (Thrastarson et al., 2024) were obtained using adjoint full waveform inversions (Fichtner, 2010; Tromp, 2025) and also include radial anisotropy. We, on the other hand, ignored the effects of P-wave anisotropy, as did DETOX-P3. Given the paucity of Pn wave data in the oceans, where radial (and azimuthal) anisotropy has been known to exist since the pioneering work of Hess (1964), we have no hope of resolving P-wave anisotropy at a global scale. In the inversion for model REVEAL horizontal and vertical V_P were essentially enforced to be the same (Thrastarson, pers. comm., 2025) indicating even radial anisotropy is not robustly resolvable. Visual comparison of vertical and horizontal V_P of model GLAD-M35 showed no perceptible difference either.

The resolution obtained for these P-wave models is comparable to that of UNICA25 shown in Fig. 7 and 8 except near Polynesia, where the MERMAID data provide much needed constraints, improving resolving power certainly in the upper half of the mantle. Cui et al. (2024) present approximate resolution results for GLAD-M35 showing resolution lengths for V_P of the order of 200-300 km in the upper mantle and 400-500 km at deeper

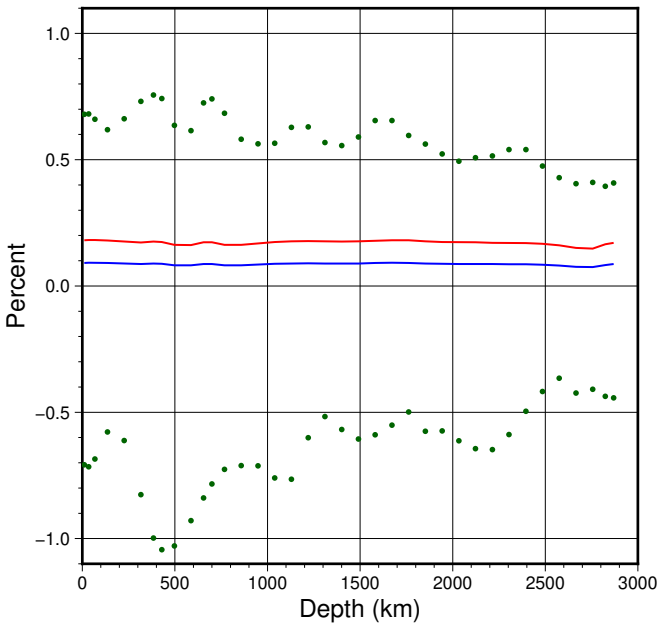

Figure 9 Inverting a data vector of pure noise allows us to estimate the propagation of errors in the inversion as a function of depth. The blue line shows the standard deviation of the distribution of V_P anomalies, the red line gives the 95% confidence level. Green dots indicate the minimum and maximum value found in individual voxels.

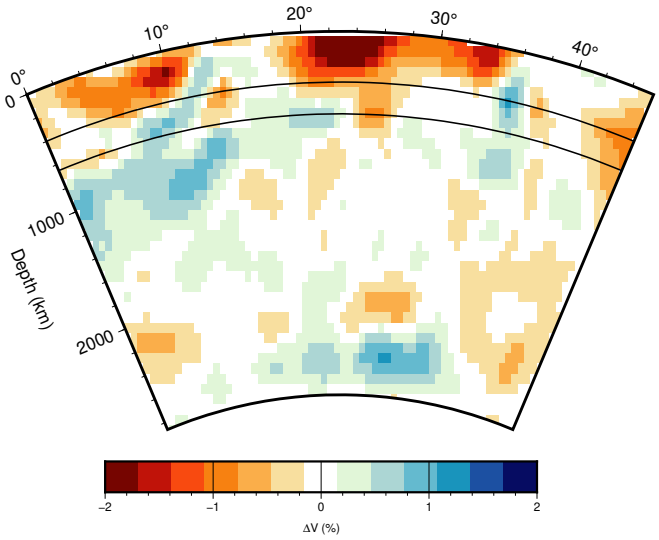

Figure 10 Model UNICA25 over the same cross-section as Fig. 1. Solid lines mark the discontinuities at 410 and 660 km depth.

levels. Similarly, DETOX-P3 shows a good response to Gaussian anomalies with $R_e = 300$ km. That we obtain comparable or better resolution with respect to FWI is unquestionably due to the fact that we used the finite-frequency kernels of Dahlen et al. (2000) at much higher frequencies than used for GLAD-M35 (< 0.06 Hz) or REVEAL (< 0.03 Hz), and that these were combined with onset time picks that satisfy ray theory, essentially infinite frequency.

Another advantage of our approach is that the computational effort – less than 12 hours CPU time on 30 nodes of a small cluster for 5000 iterations: 360 CPU hours is trivial when compared to that needed for FWI. Even Thrastarson et al. (2024), who employed clever optimization schemes to reduce the computational costs for FWI, needed 460 072 Graphical Processing Unit hours on a Cray XC50 for 305 iterations. The first 15 iterations of the GLAD series consumed more than 6 million GPU-hours (Bozdag et al., 2016). Linearized inversion, with periods down to 2 s, is at least 1000 times faster than optimized inversion down to 30 s period, and close to five orders of magnitude faster than the time needed to reach a lowest period of 17 s as in GLAD-M35. We use only body waves, and did not invert for shear wave velocity variations or anisotropy. But adding V_S tomography – for which data are less abundant – would not even double our computational effort. Nor would adding anisotropy have affected the observation that the CPU efforts are hugely different.

Compared to other inversion methods there are other notable differences: both onset 'picks' and waveform delays observed by cross-correlation are corrected for station elevation and include bathymetry corrections at pP and PP reflection points, and we are able to compute predicted travel times using a 3D crust as background model, which is straightforward using ray theory, whereas the neglect of surface topography and ocean/continent transitions in forward modelling constitutes a problem for surface wave inversions (Zheng et al., 2024). The FWI approach does incorporate surface topography, but uses an approximate 'ocean load' to include the effect of the water layer.

Since we gain more than three orders of magnitude in CPU time with respect to the fastest FWI effort, it is worthwhile to compare the results of both approaches. We compare the models in Fig. 11, which shows how the anomalies, as averaged over the voxels of $\mathbf{m}$ (see below), differ between the models. It is clear that the three models differ significantly. Not only are the FWI models much smoother than UNICA25, they show large differences between themselves, especially in the upper mantle. Differences between the FWI models are to be expected since they are based on different frequency windows, but some differences may be due to disagreements between the numerical codes used to predict the waveforms (Fichtner, pers. comm., 2025).

We decided to investigate how well the FWI models satisfy our data set. Not only does this represent a test against completely independent data, but the majority of these delays – the EHB set – have stood the test of time and also have reliable standard errors. To compute misfits, we project the FWI models on our grid by sampling all available grid points within each voxel and average the differences with the background model to obtain the model value m_i for voxel i. This value is substituted in $\mathbf{m}$ and we compute the predicted delay $\mathbf{d}_{\mathrm{FWI}} = \mathbf{A}\mathbf{m}$ which is then compared to the observed data. The projection is not trivial in the presence of ellipticity and topography on discontinuities (see Appendix).

Because there is a trade-off between source corrections and upper mantle heterogeneity, we adapt the source corrections for each FWI model separately, such that their fit to the data is optimized. For GLAD-M35 this gave acceptable RMS average source corrections of

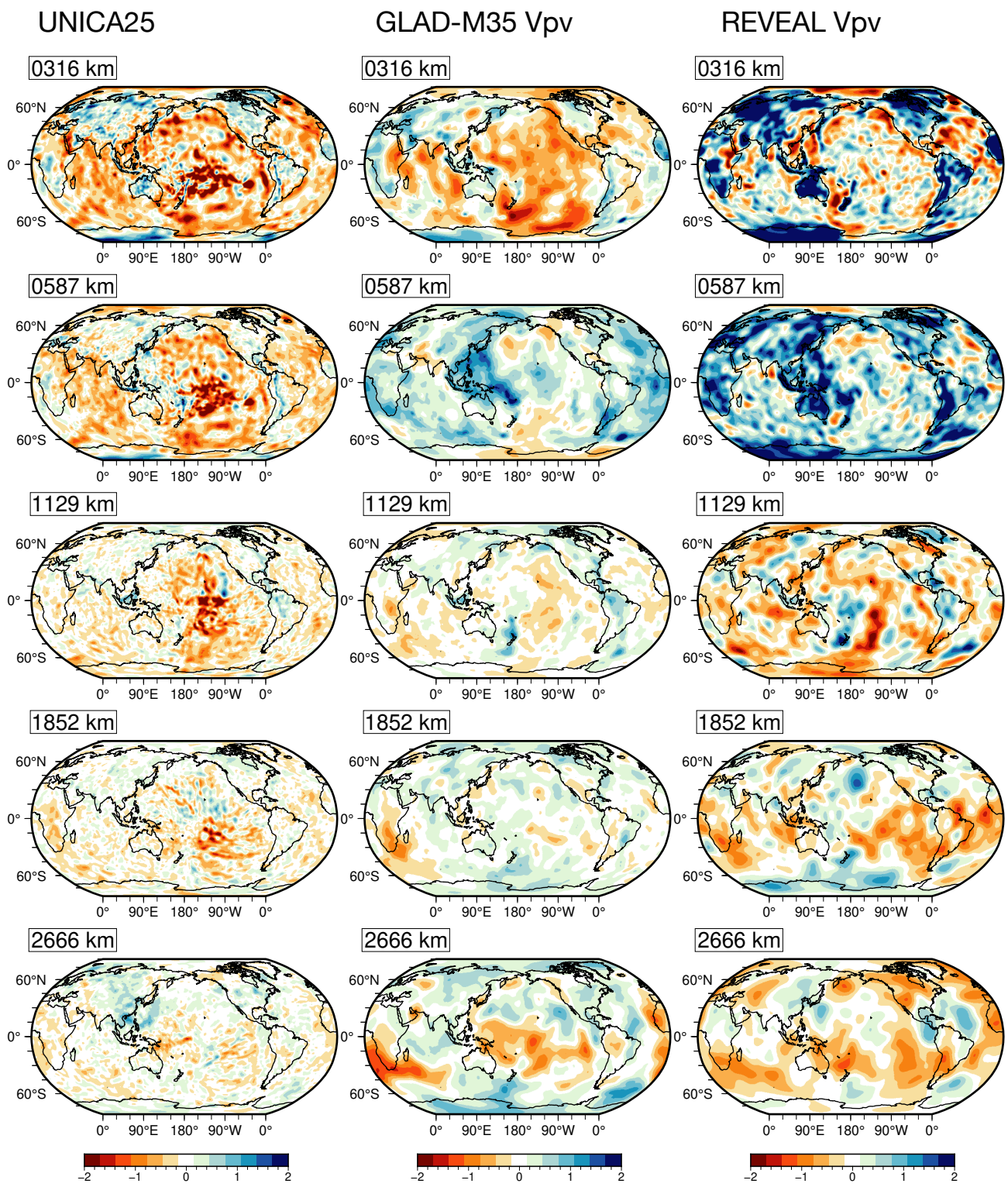

Figure 11 Model UNICA25 compared to FWI models GLAD-M35 and REVEAL in the mantle. The difference with model AK135 (and LITHO1.0 crust) is in per cent. The velocity anomalies plotted here are the averages over the voxels that are the elements of the model vector $\mathbf{m}$. See the Appendix for details on the conversion from absolute velocity to velocity anomaly for the FWI models.

1.1 s in origin time and 22 km in depth, longitude and latitude. For REVEAL, the RMS corrections were 1.0 s and 20 km, respectively. Table 3 compares the χ^2_d for the data subsets and each of the models.

Model GLAD-M35 fits the full data set with $\chi^2_\mathrm{d} = 2.64$, and REVEAL has $\chi^2_\mathrm{d} = 3.32$, which are both worse than the $\chi^2_\mathrm{d} = 0.98$ of UNICA25. Such deviation from 1 may be acceptable if the data errors are underestimated, by a factor of $\sqrt{2.64} = 1.6$ or $\sqrt{3.32} = 1.8$, respectively. This is certainly not the case of the EHB data, for which objective statistics on the errors are available (Nolet and van der Lee, 2022; Nolet, 2023), but may be a factor to consider for the other arrivals. In fact, a look at the numbers for individual data sets shows REVEAL to sat-

isfy the EHB-P data with $\chi^2_{\rm d} = 1.7$, and both models show a RMS misfit $|\Delta t|_{\rm av}$ for P-delays in seconds that is only slightly worse than UNICA25. This difference can probably be explained by the lack of small scale detail in the lower mantle of the FWI models.

We also added the depth-averaged RMS anomaly and signed average of these models to Fig. 6. In the lower mantle, all models stay close to AK135, with the depth average slightly positive for GLAD-M35 and negative for the other two. Since AK135 was derived from ISC-EHB data, one expects that close agreement with AK135 of the averages is needed to satisfy that part of our data set. The RMS variations are a factor two larger in REVEAL than for the other two. Much larger are the differences in the upper mantle. GLAD-M35 has an average of +0.4% for the voxels centered at 587 km depth, and +2.3% at 655 km. REVEAL, on the other hand, has +0.7% at 587, and -1.2% at 655, while UNICA25 stays close to zero. The RMS variations for both FWI models in the upper mantle are significantly larger than those of UNICA25. We thus expect relatively large differences in phases such as the phase labeled 'Pn' (bottoming above the 410 km discontinuity) or pP.

We suspect that the oscillating peaks, exceeding 1%, in the average velocity near the upper mantle discontinuities shown in Fig. 6 are an artefact of keeping the discontinuity depths fixed during inversion. FWI is far more sensitive to discontinuity depth than our data set of diving waves, since the waveforms include full triplications as well as reverberations. If the depth is fixed, FWI may try to fit them by including velocity changes above the discontinuity, which must be compensated below the discontinuity in order to fit the arrival time of the deeper reaching P waves. This would also explain why the misfit for both models to P waves bottoming above the transition zone (labeled Pn by ISC-EHB) is large, with $\chi^2_{\rm d} = 9.9$ and 12.3. The average misfit shows that it is significantly positive for GLAD-M35, which has variable topography, and negative for REVEAL which has fixed interfaces at 410 and 660 km depth. A similar difference in sign of the average delay is observed for the PKP phases.

Near the CMB (Figs. S10 and S20) our model is reduced to very small short-wavelength anomalies with amplitude that is not only below that of the other tomographic P-wave models, perhaps indicating that our approximate ray-theoretical treatment of P diffracted waves is flawed.

6 Conclusions

We have inverted a large and well-distributed number of travel-time anomalies to derive a new tomographic model, UNICA25: we used more than 10 million delay times (not counting that the EHB summary data were derived from more than 35 million delay times). The EHB data – which constitute 85% of our total data set – come with objectively determined standard errors, and we took great care to have solid error estimates for the others, which enabled us to find an optimal degree of regularization, yielding $\chi^2 = 0.98$, or an average fit of the data equal to $\sqrt{0.98} = 0.99$ times the standard errors.

Using onsets combined with dispersive P-wave delays at short and intermediate periods the model has high resolution in the northern hemisphere lower mantle (300 km or better), and even in some parts of the southern hemisphere. UNICA25 has a better fit to the delays than either GLAD-35M or REVEAL, and required only a minuscule effort of computing power in comparison. This, and the fact that the FWI models differ significantly among themselves, indicates that full waveform inversions could benefit from including onset time delays, in particular the massive ISC-EHB set. Since their sensitivities can be linearized and are computable with ray theory, adding their misfit to the penalty functions would add little to the CPU time needed for full waveform inversions.

7 Appendix A: Treatment of GLAD-M35 and REVEAL

Both GLAD-M35 and REVEAL are publicly available in netCDF file format from https://ds.iris.edu/ds/products/emc-earthmodels/. These files list V_P at discrete depth levels. But since the depth to the Moho and (in the case of GLAD-M35) of upper-mantle discontinuities varies geographically, we must be careful taking the difference between V_P of these models and that of the background model at the same depth if the depths to the discontinuities differ. Whenever the FWI models show a V_P that is on a discontinuity in the background model, we face a choice between the difference on the upper- or lower side. Or if for example the Moho depths differ, we risk comparing a mantle velocity with a crustal velocity and find a large difference that is not representative over a larger depth interval.

If there is only one FWI grid point within a voxel of our $\mathbf{m}$, we risk spreading the large difference over the whole voxel, whereas in reality the anomalous velocity only influences a much smaller depth interval. In the top 9 km of the crust we avoid comparison with the ocean layer or with very thin sedimentary layers, which may give unreasonable large $\Delta V_P/V_P$, but define the difference instead with a nearby LITHO1.0 layer below or above, whichever gives the smallest difference. A similar situation arises at the upper mantle discontinuities. Model S362ANI (Kustowski et al., 2008), which was used as a starting model for the GLAD series of models, has a topography near 660 km depth that is at most 15 km and usually smaller, but the voxels embracing the 655 km and 410 km depth levels have a thickness of 45 km. Thus, if there were only grid point in the voxel, it would cause an average travel time anomaly for that deflection of the interface that is wrong by an order of magnitude. It is therefore important to have a number of grid points in each voxel, spread over its depth, such that the average anomaly reflects their influence accurately.

For GLAD-M35 we obtained the full grid used in the computations (Cui, pers. comm., 2025), which has about 100 grid points in each voxel of $\mathbf{m}$. This presents no problem, as the average anomaly will represent a true average. For REVEAL, we obtained a dense netCDF file

(Thrastarson, pers. comm., 2025) that has a 5 km depth spacing inside the transition zone and we interpolated the lower mantle at 10 km depth intervals to assure a representative average within the voxels.

To compute the misfit for the GLAD-M35 grid, which specifies radius r rather than depth, we determine the depth in the ellipsoidal Earth using the Radau approximation for ellipticity, as this is what was used for the model (Tromp, pers. comm., 2025; Dahlen and Tromp (1998)). REVEAL is already defined by depth rather than radius, and we adopted this as the depth in the spherical Earth.

The projection using averaging on the voxels involves by necessity a smoothing, but it is clear from Fig. 11 that the FWI models are already quite smooth and any modifications introduced are much smaller than the large differences between the models themselves and should not have large consequences for the misfits listed in Table 3. The largest differences are in the crust and lithosphere, where a P-wave spends of the order of 20 s. The average difference with AK135 is there about 3% (Fig. 6), equivalent to a delay of 0.6 s. Any error in the averaging can only be a fraction of this, but even if it were half the difference (0.3 s) this would have only a minor effect on χ^2_{d}.

Acknowledgements

We gratefully acknowledge discussions with Jeroen Tromp, Sölvi Thrastarson and Andreas Fichtner. Congyue Cui and Sölvi Thrastarson provided densely sampled versions of their FWI models. I.S., S.B. and G.N. were supported by ERC project Globalseis (advanced grant 226837). A proof-of-concept addition to this grant financed the development of the MERMAID floats. Ifremer (France) and JAMSTEC (Japan) provided the shiptime for launching SPPIM floats (doi: 10.17600/18000882, doi: 10.17600/18000519 and doi: 10.17596/0002686). J. D. S. was supported by National Science Foundation (NSF) Grant Numbers OCE-1917058 and EAR-2341811 to Frederik J. Simons and Jessica C.E. Irving. The Japanese contribution to SPPIM, including 9 MERMAIDs, was financed through JSPS KAKENHI Grant 19H00731. Princeton financed 16, and SUSTech financed 23 of the MERMAID floats. K.S., D.N. and S.B were supported by the UCAJEDI Investments in the Future project (reference ANR-15-IDEX-01). We used GMT6 (Wessel et al., 2019) and SubMachine (Hosseini et al., 2018) for plotting. The comments of two anonymous reviewers were very helpful in clarifying some issues in the original version of this paper.

Data and code availability

The inversion software is available from https://www.geoazur.fr/GLOBALSEIS/Soft.html. The summary data used here (Nolet, 2023) are accessible via de ISC Products website: http://www.isc.ac.uk/dataset_repository/ or https://doi.org/10.31905/MPPIDWHM. The full ISC-EHB data set (Weston et al., 2018; Engdahl et al., 2020; International Seismological Centre, 2020) is available from http://www.isc.ac.uk/isc-ehb/. The MERMAID metadata and seismograms are available at the EarthScope Consortium data management centre (https://www.earthscope.org/; formerly Incorporated Research Institutions for Seismology [IRIS]) under the network code "MH" (doi: 10.7914/SN/MH). With a few exceptions (floats P0006, P0007, P0008, P0010, and P0016) these seismograms are embargoed for two years after acquisition. For the other data sets please contact the first author (nolet@princeton.edu). All websites were last accessed on December 1, 2025. Model UNICA25 is available at the new Submachine location: https://orfeus-eu.org/submachine/index.php.

Competing interests

The authors have no competing interests.

References

Adams, R., Hughes, A., and McGregor, D. Analysis procedures at the International Seismological Centre. *Phys. Earth Planet. Inter.*, 30:85–93, 1982. doi: 10.1016/0031-9201(82)90093-0.

Amaru, M. L. *Global travel time tomography with 3-D reference models*. PhD thesis, Utrecht University, 2007.

Bijwaard, H. and Spakman, W. Non-linear global P-wave tomography by iterated linearized inversion. *Geophys. J. Int.*, 141:71–82, 2000. doi: 10.1046/j.1365-246X.2000.00053.x.

Bonnin, M., Nolet, G., Villasenor, A., Gallart, J., and Thomas, C. Multiple-frequency tomography of the upper mantle beneath the African/Iberian collision zone. *Geophys. J. Int.*, 198: 1458–1473, 2014. doi: 10.1093/gji/ggu214.

Boschi, L. and Dziewonski, A. High- and low-resolution images of the Earth's mantle: implications of different approaches to tomographic modeling. *J. Geophys. Res.*, 104:25567–25594, 1999. doi: 10.1029/1999JB900208.

Bozdag, E., Peter, D., Lefebvre, M., Komatitsch, D., Tromp, J., Hill, J., Podhorszki, N., and Pugmire, D. Global adjoint tomography: first generation model. *Geophys. J. Int.*, 207:1739–1766, 2016. doi: 10.1093/gji/ggw356.

Charléty, J., Voronin, J., Nolet, G., Loris, I., Simons, F., and Daubechies, I. Global seismic tomography with sparsity constraints: Comparison with smoothing and damping regularization. *J. Geophys. Res.*, 118, 2013. doi: 10.1002/jgrb.50326.

Cui, C., Lei, W., Liu, Q., Peter, D., Bozdag, E., Tromp, J., Hill, J., Podhorszki, N., and Pugmire, D. GLAD-M35: a joint P and S global tomographic model with uncertainty quantification. *Geophys. J. Int.*, 239:478–502, 2024. doi: /10.1093/gji/ggae270.

Dahlen, F. and Tromp, J. *Theoretical Global Seismology*. Princeton Univ. Press, Princeton NJ, 1998.

Dahlen, F., Hung, S.-H., and Nolet, G. Fréchet kernels for finite-frequency traveltimes – I. Theory. *Geophys. J. Int.*, 141:157–174, 2000. doi: 10.1046/j.1365-246X.2000.00070.x.

Dziewonski, A., Hager, B., and O'Connell, R. Large-scale heterogeneities in the lower mantle. *J. Geophys. Res.*, 82:239–255, 1977. doi: 10.1029/jb082i002p00239.

Eilon, Z., Zhang, L., Gaherty, J., Forsyth, D., and Russell, J. Sub-Lithospheric Small-Scale Convection Tomographically Imaged Beneath the Pacific Plate. *Geophys. Res. Lett.*, 49: e2022GL100351, 2022. doi: 10.1029/2022GL100351.

Engdahl, E., van der Hilst, R., and Buland, R. Global teleseismic earthquake relocation with improved travel times and pro-

cedures for depth determination. *Bull. Seismol. Soc. Am.*, 88: 722–743, 1998. doi: 10.1785/BSSA0880030722.

Engdahl, E., Giacomo, D. D., Sakarya, B., Gkarlaouni, C., Harris, J., J., and Storchak, D. ISC EHB1964-2016, an improved data set for studies of Earth structure and global seismicity. *Earth and Space Sci.*, 7:e2019EA000897, 2020. doi: 10.1029/2019EA000897.

Fichtner, A. *Full Seismic Waveform Modelling and Inversion*. Springer, Heidelberg, 2010.

Fukao, Y. and Obayashi, M. Subducted slabs stagnant above, penetrating through, and trapped below the 660 km discontinuity. *J. Geophys. Res.*, 118:5920–5938, 2013. doi: 10.1002/2013JB010466.

Hall, R. and Spakman, W. Mantle structure and tectonic history of SE Asia. *Tectonophys.*, 658:14–45, 2015. doi: 10.1016/j.tecto.2015.07.003.

Hello, Y. and Nolet, G. Floating Seismographs (MERMAIDS). In Gupta, H. K., editor, *Encyclopedia of Solid Earth Geophysics*, pages 1–6. Springer International Publishing, 2020. doi: 10.1007/978-3-030-10475-7_248-1.

Hello, Y., Ogé, A., Sukhovich, A., and Nolet, G. Modern Mermaids: new floats image the deep Earth. *EOS Trans. Am. Geophys. Un.*, 92:337–338, 2011. doi: 10.1029/2011EO400001.

Hess, H. Seismic anisotropy of the uppermost mantle under the oceans. *Nature*, 203:629–631, 1964. doi: 10.1038/203629a0.

Hosseini, K. and Sigloch, K. Multifrequency measurements of core-diffracted P waves (Pdiff) for global waveform tomography. *Geophys. J. Int.*, 203:506–521, 2015. doi: 10.1093/gji/ggv298.

Hosseini, K., Matthews, K., Sigloch, K., Shepard, G., Domeier, M., and Tseknistrenko, M. SubMachine: Web-based tools for exploring seismic tomography and other models of Earth's deep interior. *Geochem. Geophys. Geosys.*, 19, 2018. doi: DOI 10.1002/2018GC007431.

Hosseini, K., Sigloch, K., Tsekhmistrenko, M., Zaheri, A., Nissen-Meyer, T., and Igel, H. Global mantle structure from multifrequency tomography using P, PP and P-diffracted waves. *Geophys. J. Int.*, 220:96–141, 2020. doi: 10.1093/gji/ggz394.

Hung, S.-H., Dahlen, F., and Nolet, G. Fréchet kernels for finite-frequency travel times – II. Examples. *Geophys. J. Int.*, 141: 175–203, 2000. doi: 10.1046/j.1365-246X.2000.00072.x.

International Seismological Centre. ISC-EHB dataset. *https://doi.org/10.31905/PY08W6S3*, 2020. doi: 10.31905/PY08W6S3.

Kang, H., Kim, Y., Hung, S.-H., Lin, P.-Y. P., Isse, T., Kawakatsuand, H., Lee, S.-M., Utada, H., Takeuchi, N., Sugioka, H. S. H., , and Kim, S.-S. Seismic Velocity Structure of Upper Mantle Beneath the Oldest Pacific Seafloor: Insights From Finite-Frequency Tomography. *Geochem. Geophys. Geosys.*, 24:e2022GC010833, 2023. doi: 10.1029/2022GC010833.

Kennett, B., Engdahl, E., and Buland, R. Constraints on seismic velocities in the Earth from traveltimes. *Geophys. J. Int.*, 122: 108–124, 1995. doi: 10.1111/j.1365-246X.1995.tb03540.x.

Kustowski, B., Ekström, G., and Dziewonski, A. Anisotropic shear-wave velocity structure of the Earth's mantle: a global model. *J. Geophys. Res.*, 113:B06306, 2008. doi: 10.1029/2007JB005169.

Lu, C., Grand, S., Lai, H., and Garnero, E. TX2019slab: A new P and S tomography model incorporating subducting slabs. *J. Geophys. Res.*, 124:11,549–11,567, 2019. doi: 10.1029/019JB017448.

Mercerat, E. and Nolet, G. On the linearity of cross-correlation delay times in finite-frequency tomography. *Geophys.J.Int.*, 192: 681–687, 2013. doi: 10.1093/gji/ggs017.

Montelli, R., Nolet, G., Dahlen, F., Masters, G., Engdahl, E., and Hung, S.-H. Finite-frequency tomography reveals a variety of plumes in the mantle. *Science*, 303:338–343, 2004. doi: 10.1126/science.1092485.

Montelli, R., Nolet, G., Dahlen, F., and Masters, G. A catalogue of deep mantle plumes: new results from finite-frequency tomography. *Geochem. Geophys. Geosys. (G3)*, 7:Q11007, 2006. doi: 10.1029/2006GC001248.

Nolet, G. Solving or resolving inadequate and noisy tomographic systems. *J. Comp. Phys.*, 61:463–482, 1985. doi: 10.1016/0021-9991(85)90075-0.

Nolet, G. *A Breviary of Seismic Tomography*. Cambridge Univ. Press, Cambridge, U.K., 2008.

Nolet, G. Path-averaged delay times for seismic tomography. *Geophys. J. Int.*, 235:996–1005, 2023. doi: 10.1093/gji/ggad282.

Nolet, G. and Dahlen, F. Wave front healing and the evolution of seismic delay times. *J. Geophys. Res.*, 105:19043–19054, 2000. doi: 10.1029/2000JB900161.

Nolet, G. and van der Lee, S. Error estimates for seismic body wave delay times in the ISC-EHB Bulletin. *Geophys. J. Int.*, 231: 1739–1749, 2022. doi: 10.1093/gji/ggac282.

Nolet, G., Hello, Y., van der Lee, S., Bonnieux, S., Ruiz, M. C., Pazmino, N. A., Deschamps, A., Regnier, M. M., Font, Y., Chen, Y. J., and Simons, F. J. Seismic tomography with floating seismometers: a first application to Galápagos. *Sci. Reports*, 9:1–12, 2019. doi: 10.1038/s41598-018-36835-w.

Nolet, G., Simon, J., and Bonnieux, S. How accurately are MERMAID seismograms located? *Seism. Res. Lett.*, 95:2368–2374, 2024. doi: 10.1785/0220230377.

Nolet, G., Hoang, N. B., Bonnieux, S., Kondo, Y., Kong, F., Obayashi, M., Pipatrathanporn, S., Sigloch, K., Simon, J. D., Simons, F. J., Sugioka, H., Yoshimitsu, J., and Zhang, Q. Picking first arrivals in hydroacoustic seismograms from MERMAID floats. *Seismica*, 4(1):1–12, 2025. doi: 10.26443/seismica.v4i1.1505.

Obayashi, M., Yoshimitsu, J., Nolet, G., Fukao, Y., Shiobara, H., Sugioka, H., Miyamachi, H., and Gao, Y. Finite frequency whole mantle P wave tomography: Improvement of subducted slab images. *Geophysical Research Letters*, 40(21):5652–5657, 2013. doi: 10.1002/2013GL057401.

Obayashi, M., Yoshimitsu, J., Sugioka, H., Ito, A., Shiobara, H., Reymond, D., and Suetsugu, D. Mantle plumes beneath the South Pacific superswell revealed by finite frequency P tomography using regional seafloor and island data. *Geophys. Res. Lett.*, 43: 11628–11634, 2016. doi: 10.1002/2016GL070793.

Paige, C. and Saunders, M. LSQR: An algorithm for sparse, linear equations and sparse least squares. *A.C.M. Trans. Math. Softw.*, 8:43–71, 1982. doi: 10.1145/355984.355989.

Pasyanos, M., Masters, T., Laske, G., and Ma, Z. LITHO1.0: An updated crust and lithospheric model of the Earth. *J. Geophys. Res.*, 119:2153–2173, 2014. doi: 10.1002/2013JB010626.

Pipatprathanporn, S. and Simons, F. Waveform modeling of hydroacoustic teleseismic earthquake records from autonomous MERMAID floats. *Geophys. J. Int.*, 239:136–154, 2024. doi: 10.1093/gji/ggae238.

Sigloch, K. and Nolet, G. Measuring finite-frequency body wave amplitudes and travel times. *Geophys. J. Int.*, 167:271–287, 2006. doi: 10.1111/j.1365-246X.2006.03116.x.

Simmons, N., Myers, S., Morency, C., Chiang, A., and Knapp, D. SPiRaL: a multiresolution global tomography model of seismic wave speeds and radial anisotropy variations in the crust and mantle. *Geophys. J. Int.*, 227:1366–1391, 2021. doi: 10.1093/gji/ggab277.

Simon, J., Simons, F., and Nolet, G. Multiscale estimation of event arrival times and their uncertainties in hydroacoustic records from autonomous oceanic floats. *Bull. Seismol. Soc. Am.*, 110: 970–997, 2020. doi: 10.1785/0120190173.

Simon, J., Simons, F., and Irving, J. Recording earthquakes for tomographic imaging of the mantle beneath the South Pacific by autonomous MERMAID floats. *Geophys. J. Int.*, 228:147–170, 2022. doi: 10.1093/gji/ggab271.

Simons, F., Nolet, G., Babcock, J., Davis, R., and Orcutt, J. A future for drifting seismic networks. *EOS Trans. AGU*, 31:305–307, 2006.

Simons, F., Nolet, G., Georgief, P., Babcock, J. M., Regier, L. A., and Davis, R. E. On the potential of recording earthquakes for global seismic tomography by low-cost autonomous instruments in the oceans. *J. Geophys. Res.*, 114:B05307, 2009. doi: 10.1029/2008JB006088.

Spakman, W., van der Lee, S., and van der Hilst, R. Travel-time tomography of the European-Mediterranean mantle down to 1400 km. *Phys. Earth Planet. Inter.*, 79:3–74, 1993. doi: 10.1016/0031-9201(93)90142-V.

Suetsugu, D. et al. Probing South Pacific mantle plumes with ocean bottom seismographs. *EOS Trans. AGU*, 86:429–435, 2005.

Takeuchi, N. and Kobayashi, M. Improvement of seismological earth models by using data weighting in waveform inversion. *Geophys. J. Int.*, 158:681–694, 2004. doi: 10.1111/j.1365-246X.2004.02334.x.

Thrastarson, S., van Herwaarden, D.-P., Noe, S., Schiller, C., and Fichtner, A. REVEAL: A global full-waveform inversion model. *Bull. Seismol. Soc. Am.*, 114:1392–1406, 2024. doi: 10.1785/0120230273.

Tian, Y., Hung, S.-H., Nolet, G., Montelli, R., and Dahlen, F. Dynamic ray tracing and traveltime corrections for global seismic tomography. *J. Comp. Phys.*, 226:672–687, 2007a. doi: 10.1016/j.jcp.2007.07.004.

Tian, Y., Montelli, R., Nolet, G., and Dahlen, F. Computing traveltime and amplitude sensitivity kernels in finite-frequency tomography. *J. Comp. Phys.*, 226:2271–2288, 2007b. doi: doi: 10.1016/j.jcp.2007.04.025.

Tromp, J. *Theoretical and Computational Seismology*. Princeton Univ. Press, Princeton, NJ, 2025.

van der Hilst, R., Engdahl, E., Spakman, W., and Nolet, G. Tomographic imaging of subducted lithosphere below northwest Pacific island arcs. *Nature*, 353:37–43, 1991. doi: 10.1038/353037a0.

VanDecar, J. and Snieder, R. Obtaining smooth solutions to large, linear, inverse problems. *Geophysics*, 59:818–829, 1994. doi: 10.1190/1.1443640.

Wamba, M., Simons, F., and Irving, J. Data-space cross-validation of mantle structure in global tomographic models underneath the Pacific Ocean. *Geophys. J. Int.*, 241:241–259, 2025. doi: 10.1093/gji/ggaf044.

Weatherall, P., Marks, K. M., Jakobsson, M., Schmitt, T., Tani, S., Arndt, J. E., Rovere, M., Chayes, D., Ferrini, V., , and Wigley, R. A new digital bathymetric model of the world's oceans. *Earth and Space Sc.*, 2:331–345, 2015. doi: 10.1002/2015EA000107.

Wessel, P., Luis, J., L.Uieda, Scharroo, R., Smith, W., and Tian, D. The Generic Mapping Tools version 6. *Geochem. Geophys. Geosys.*, 20:1–9, 2019. doi: 10.1029/2019GC008515.

Weston, J., Engdahl, R., Harris, J., Giacomo, D. D., and Storchak, D. ISC-EHB: Reconstruction of a robust earthquake dataset. *Geophys. J. Int.*, 214:474–484, 2018. doi: 10.1093/gji/ggy155.

Zheng, K., Wang, Y., and Zhao, L. Topography effect on seismic waveform tomography: a quantitative study. *Geophys. J. Int.*, 237:302–314, 2024. doi: 10.1093/gji/ggae041.

Zhou, Z., Gerstoft, P., and Olsen, K. B. 3D Multiresolution velocity model fusion with probability graphical models. *Bull. Seismol. Soc. Am.*, 114:14p, 2024. doi: 10.1785/0120230271.

Supplement to *A new global P-wave tomographic model of the Earth's mantle*, by G. Nolet et al.

Figs. S1-S10: Large scale versions of model UNICA25. We chose a variable colour scale (in %), such that the full colour scale corresponds to a temperature range of ±600°K as suggested by the compressional velocity derivatives $\mathrm{d}\ln V_P/\mathrm{d}T$ used by Nolet et al. (2006), which in turn were based on anharmonic derivatives for mantle rock by Wentzcovitch et al. (2004), Karato (1993), Karki et al. (1999) and Aizawa et al. (2004). The temperature derivative for postperovskite is unknown, we adopted a ±1% scale in the D" layer (Figs. S10,S20). We do not pretend that this transforms the velocity images into reliable temperature plots, since the derivatives are uncertain (certainly near the CMB) and ΔV_P is also influenced by compositional variations. The reason to vary the scale is to optimize the visibility of anomalies at each depth. We also scale the size of the figure to the true size at the depth of the plot, as indicated in km in the captions.

Figs. S11-S20: As Figs. 1-10, but centered on 0°E.

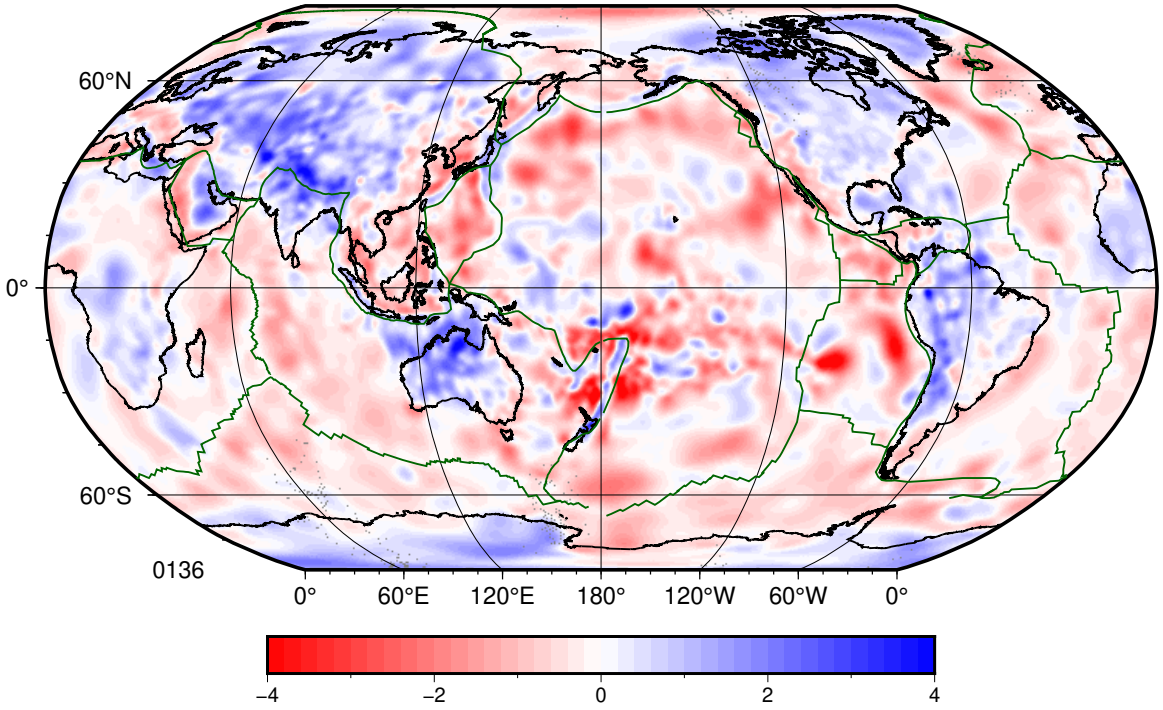

Depth 136 km.

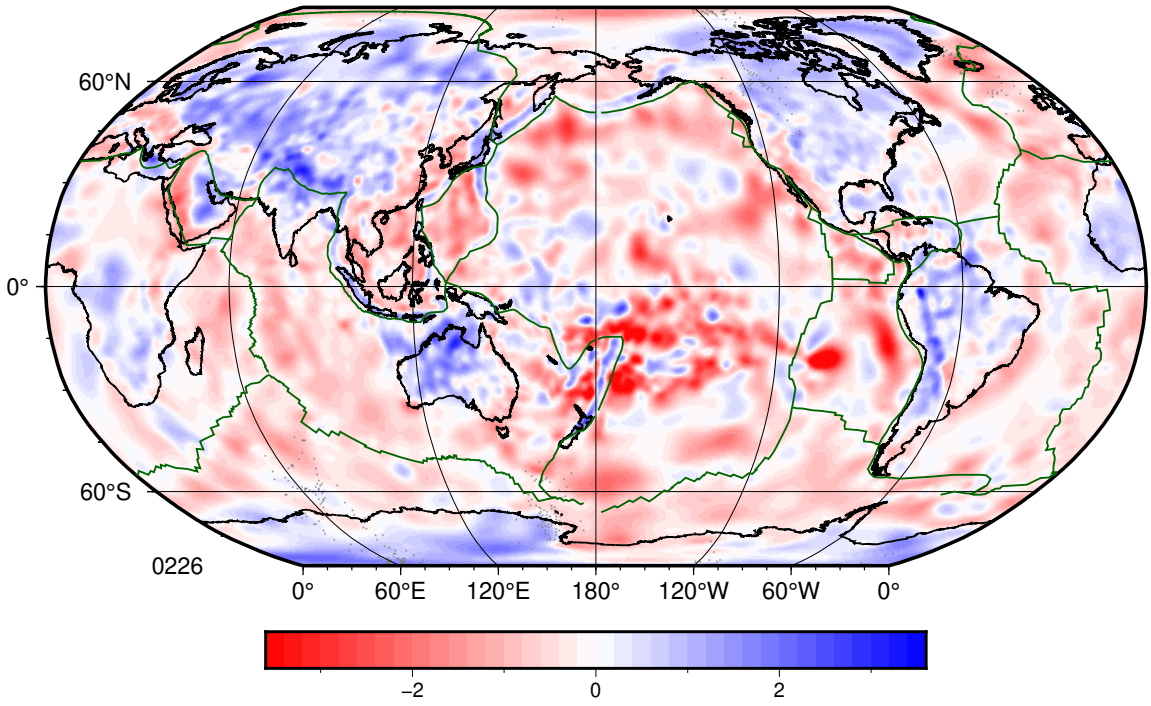

Depth 226 km.

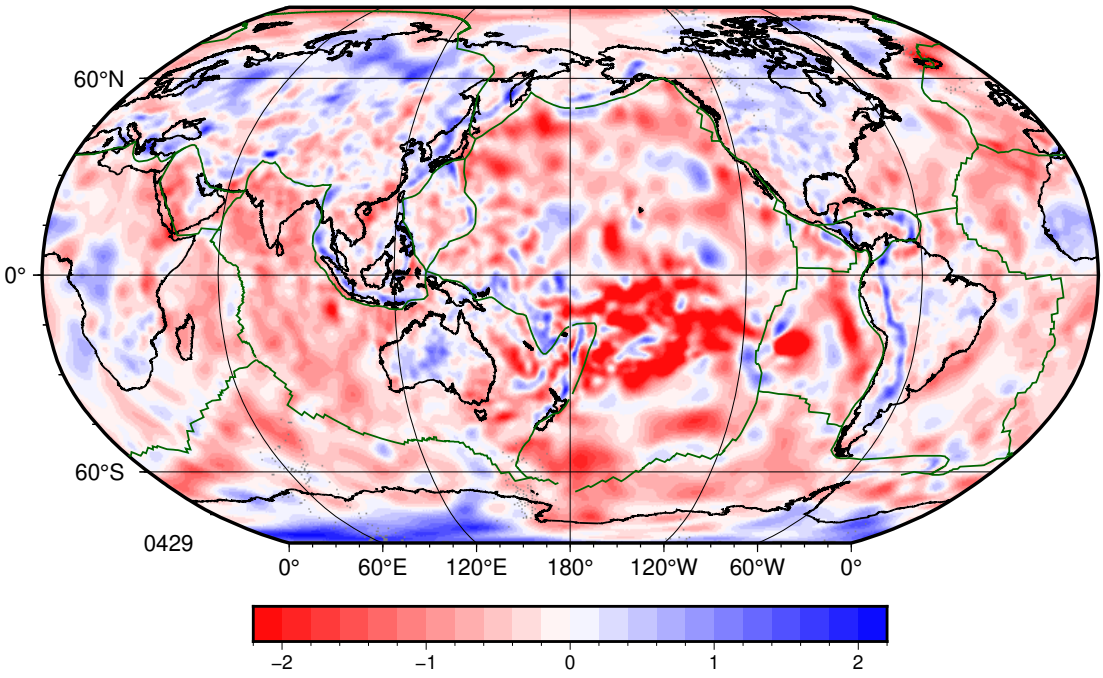

Depth 429 km.

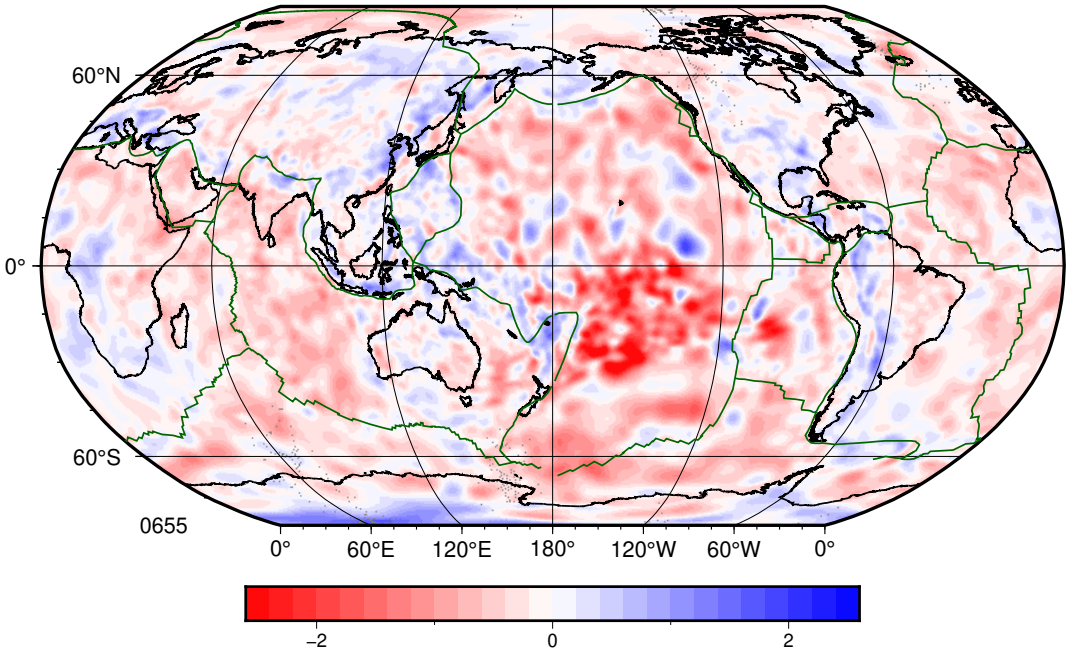

Depth 655 km.

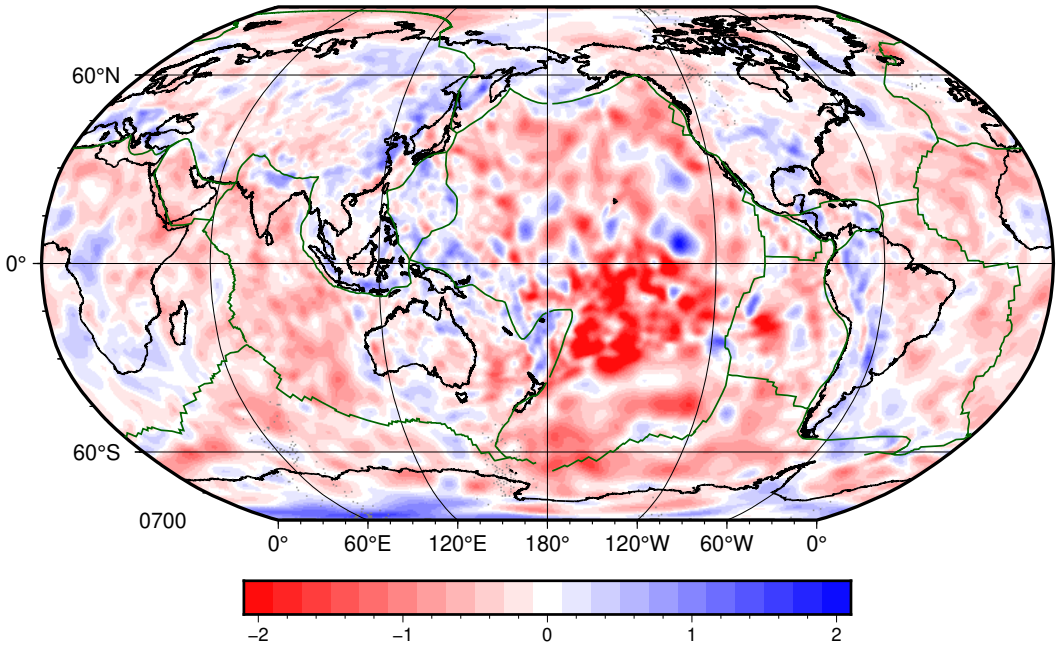

Depth 700 km.

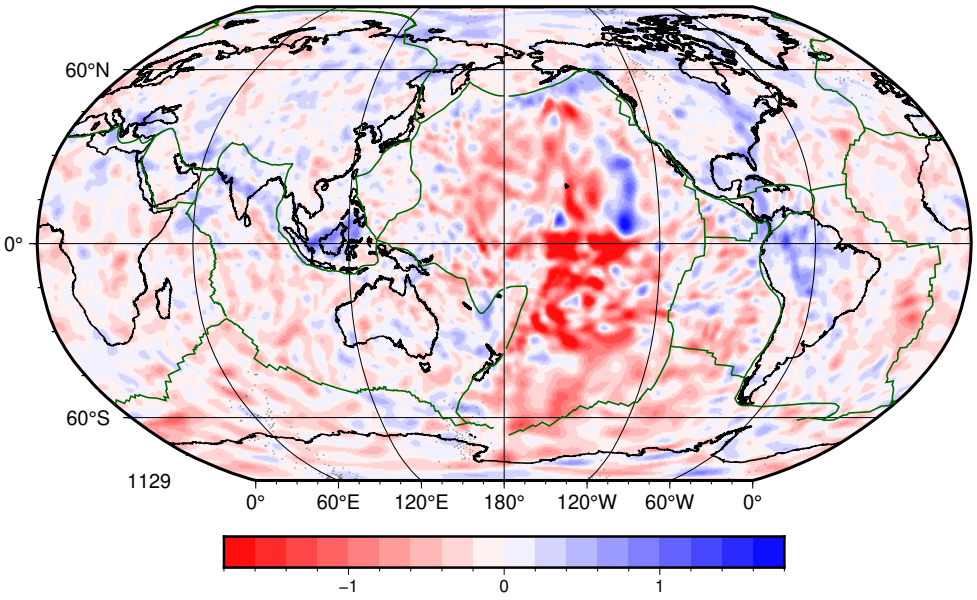

Depth 1129 km.

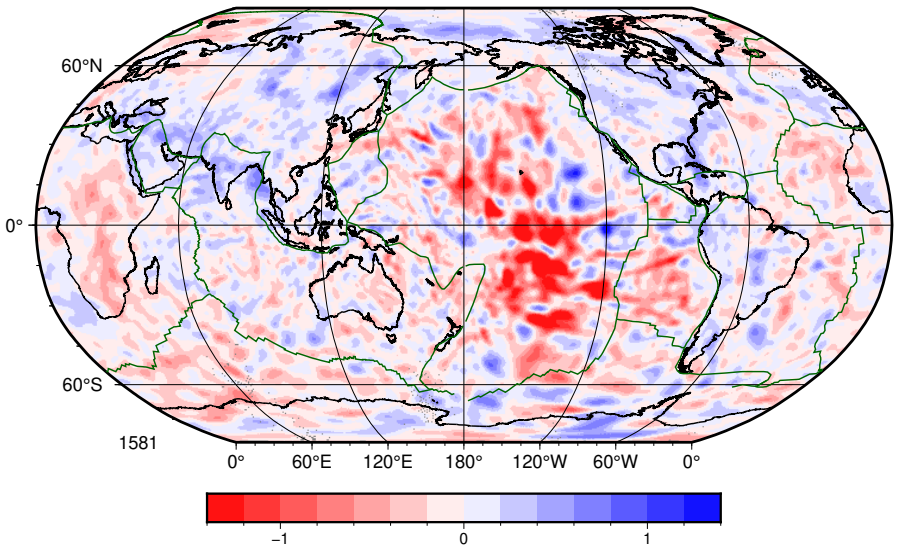

Depth 1581 km.

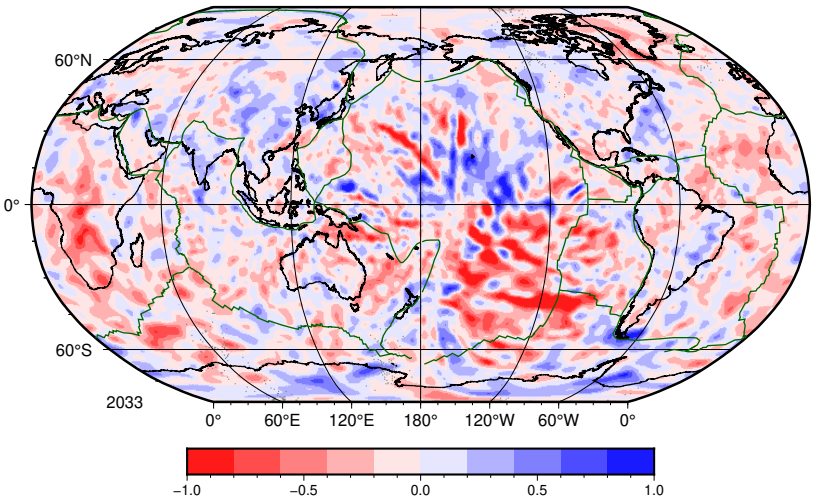

Depth 2033 km.

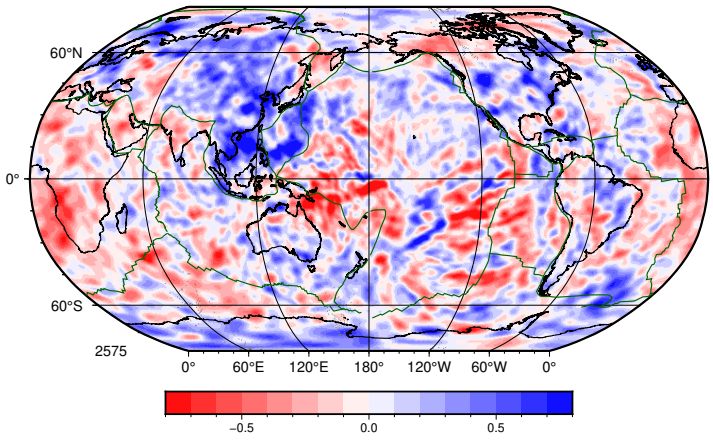

Depth 2575 km.

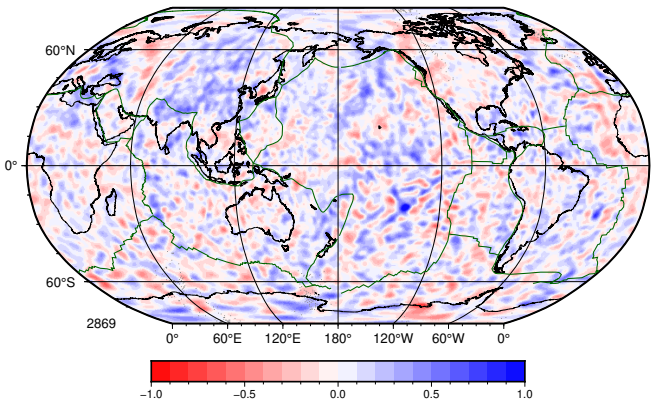

Depth 2869 km.

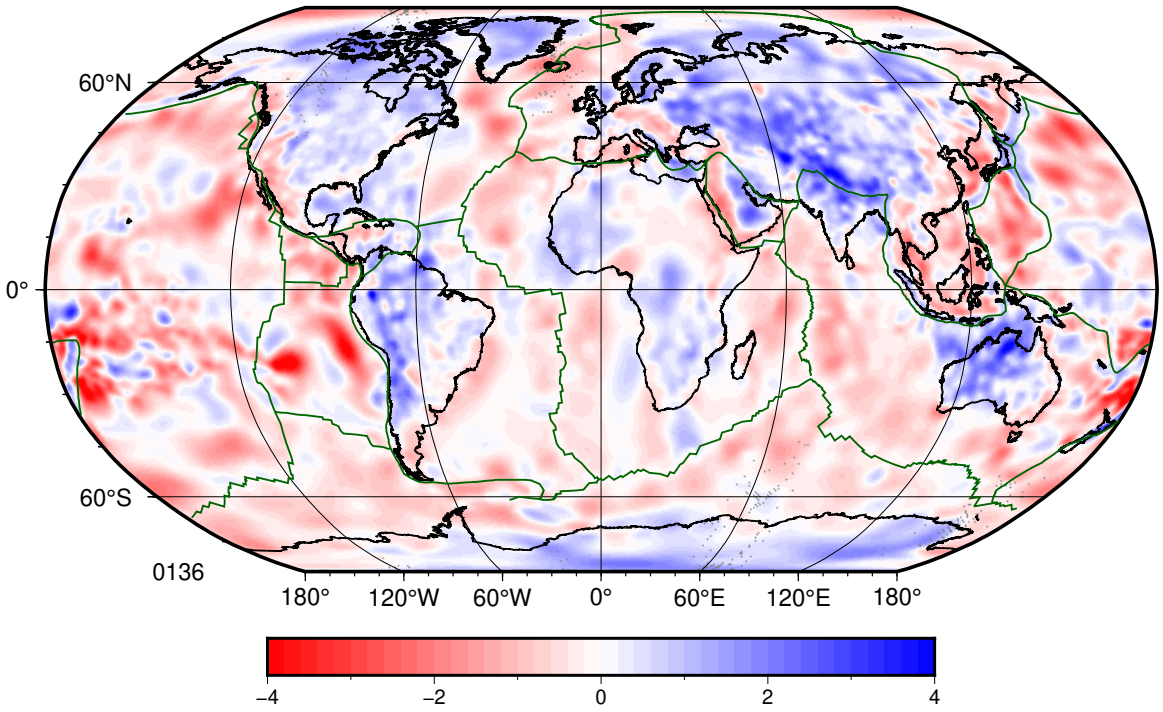

Depth 136 km.

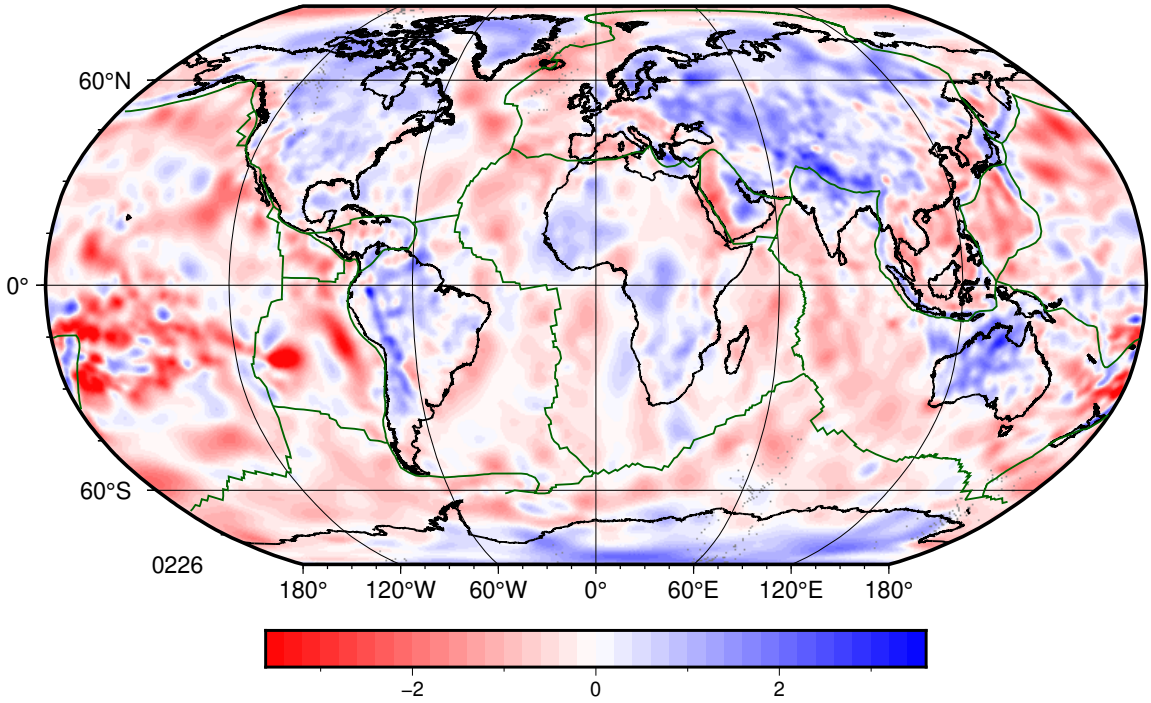

Depth 226 km.

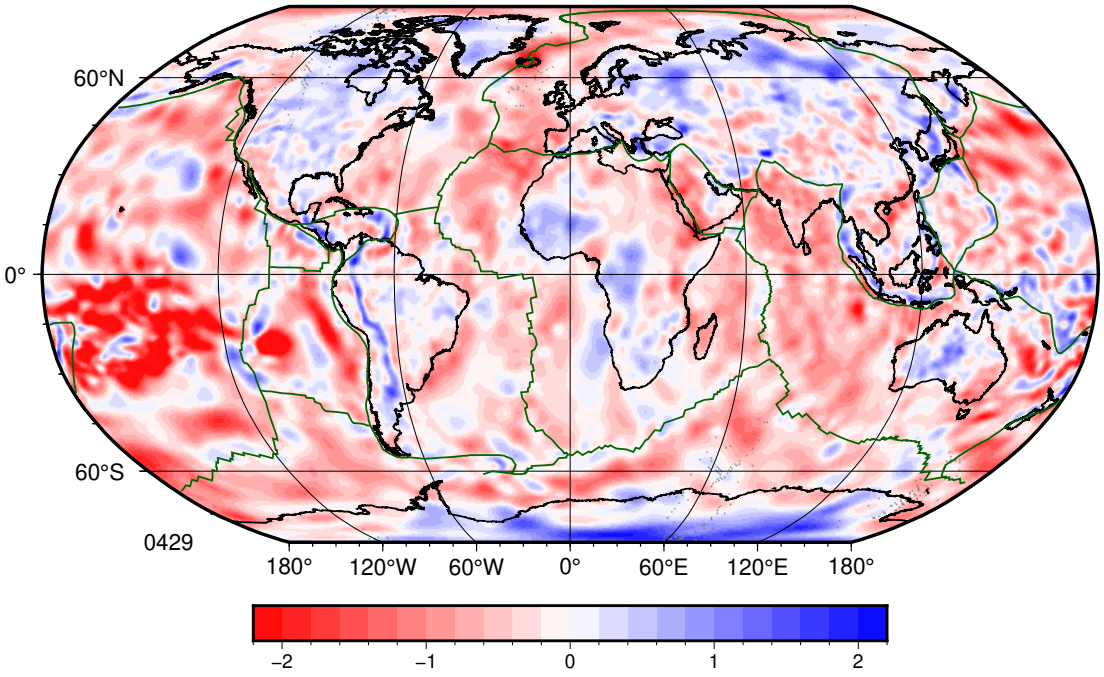

Depth 429 km.

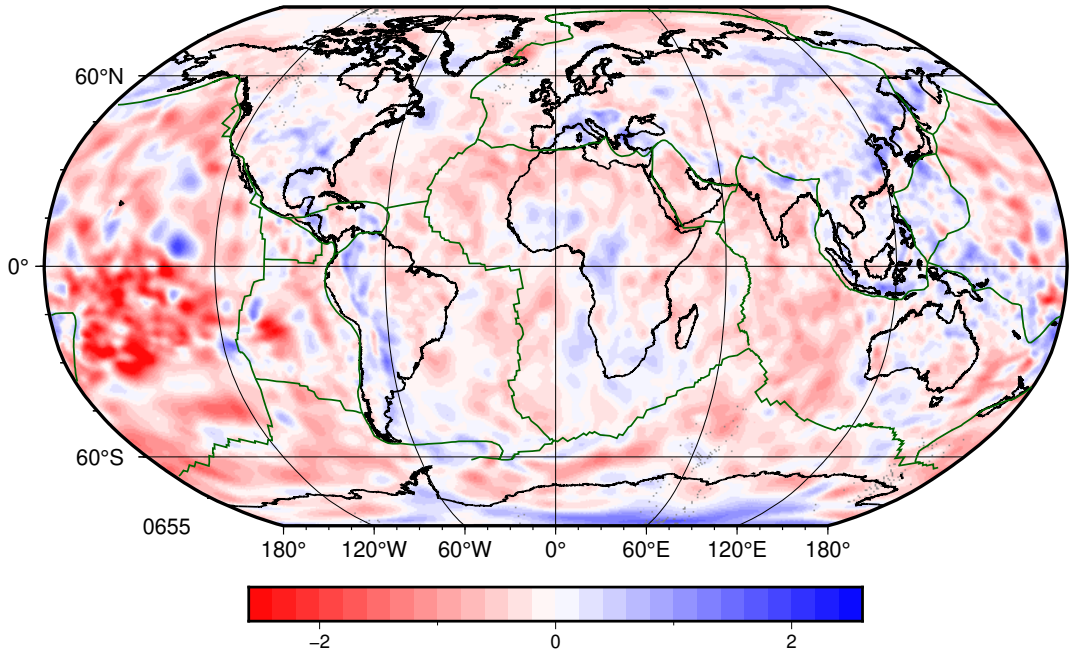

Depth 655 km.

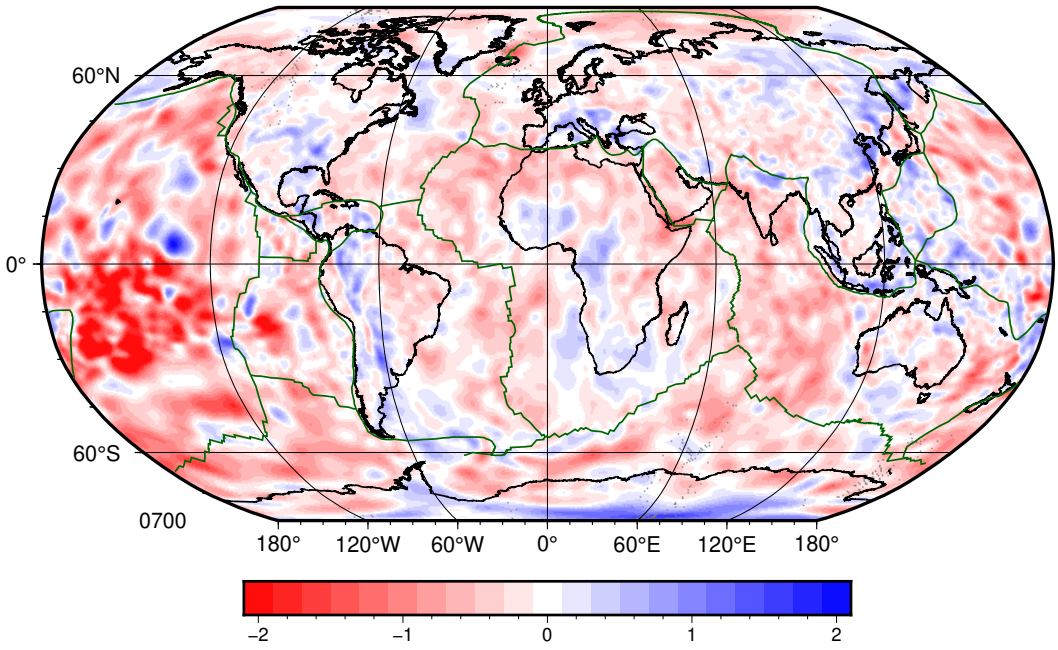

Depth 700 km.

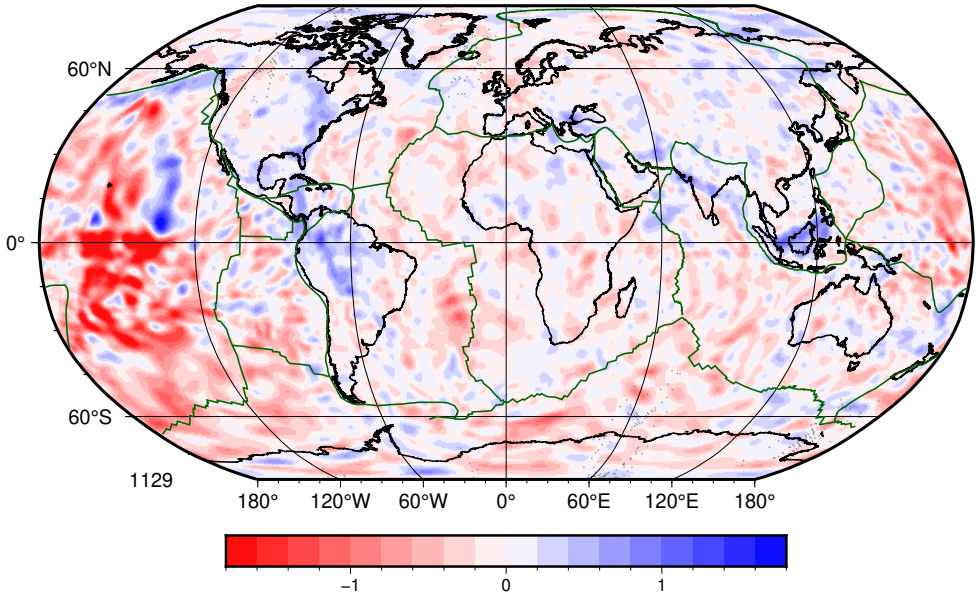

Depth 1129 km.

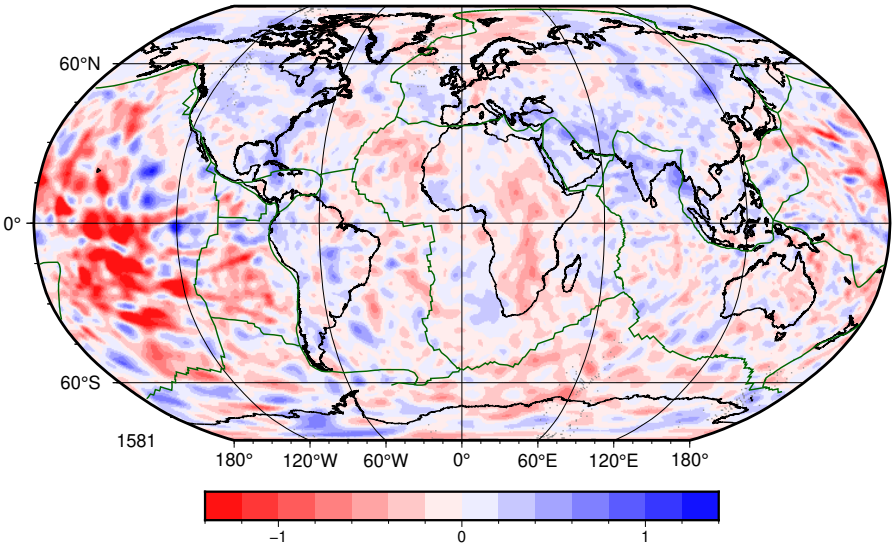

Depth 1581 km.

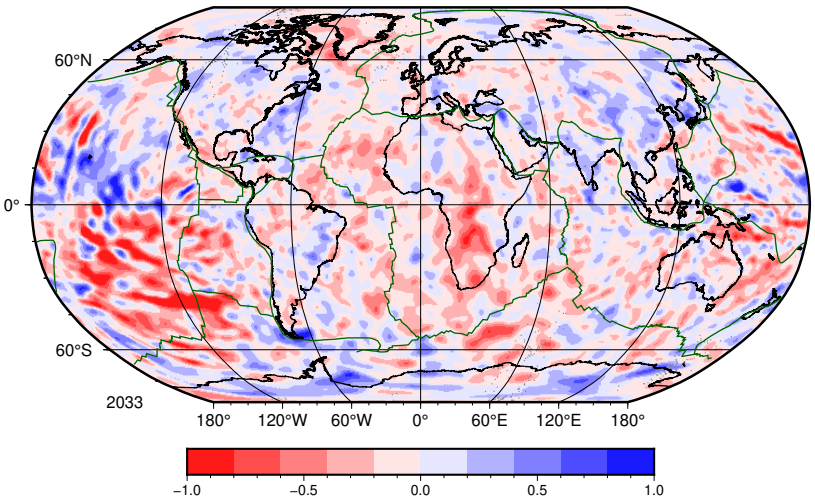

Depth 2033 km.

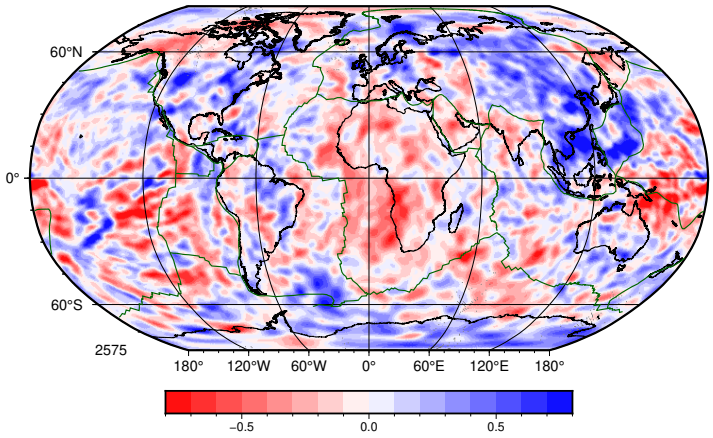

Depth 2575 km.

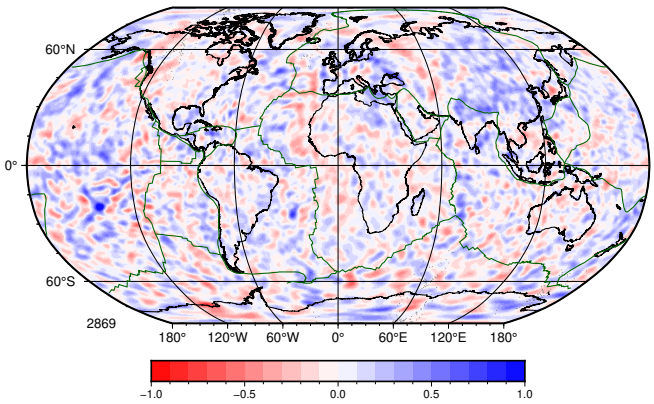

Depth 2869 km.

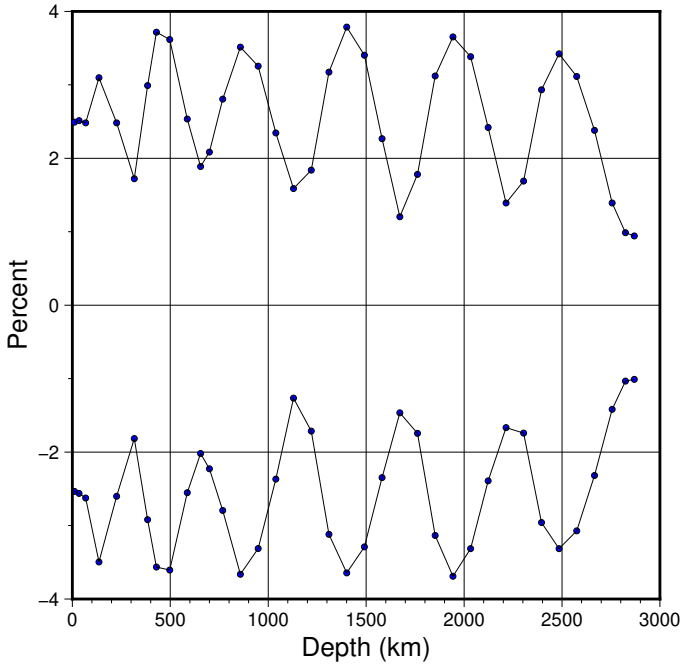

Figure S21: Minimum and maximum anomaly as a function of depth found in the results of the resolution test with 250 km Gaussian spheres. The input spheres had a maximum anomaly of 4%, showing a slight loss of amplitude (for the best resolved areas) that is mostly constant in the lower mantle near 3.5%, except near the very deepest level and near the surface.

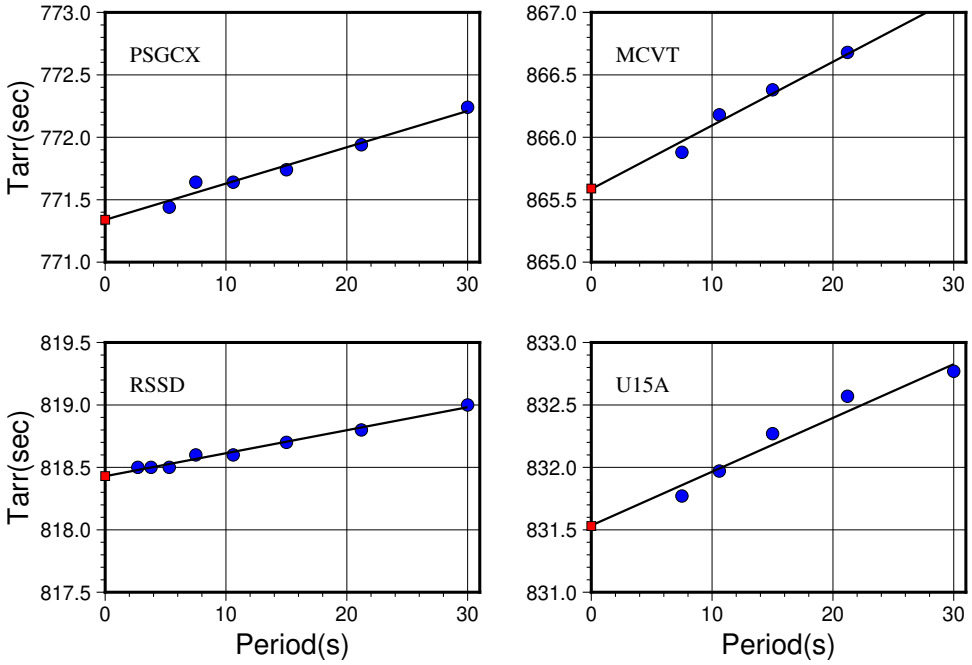

Figure S22: Examples of accepted linear fits to P diffracted dispersion for four different events in four different stations, showing different qualities of fit. Blue dots indicate observed arrival time. A regression algorithm, taking into account the formal errors of each measurement, is used to model the dispersion with a linear fit, which is sampled at zero period (red square).

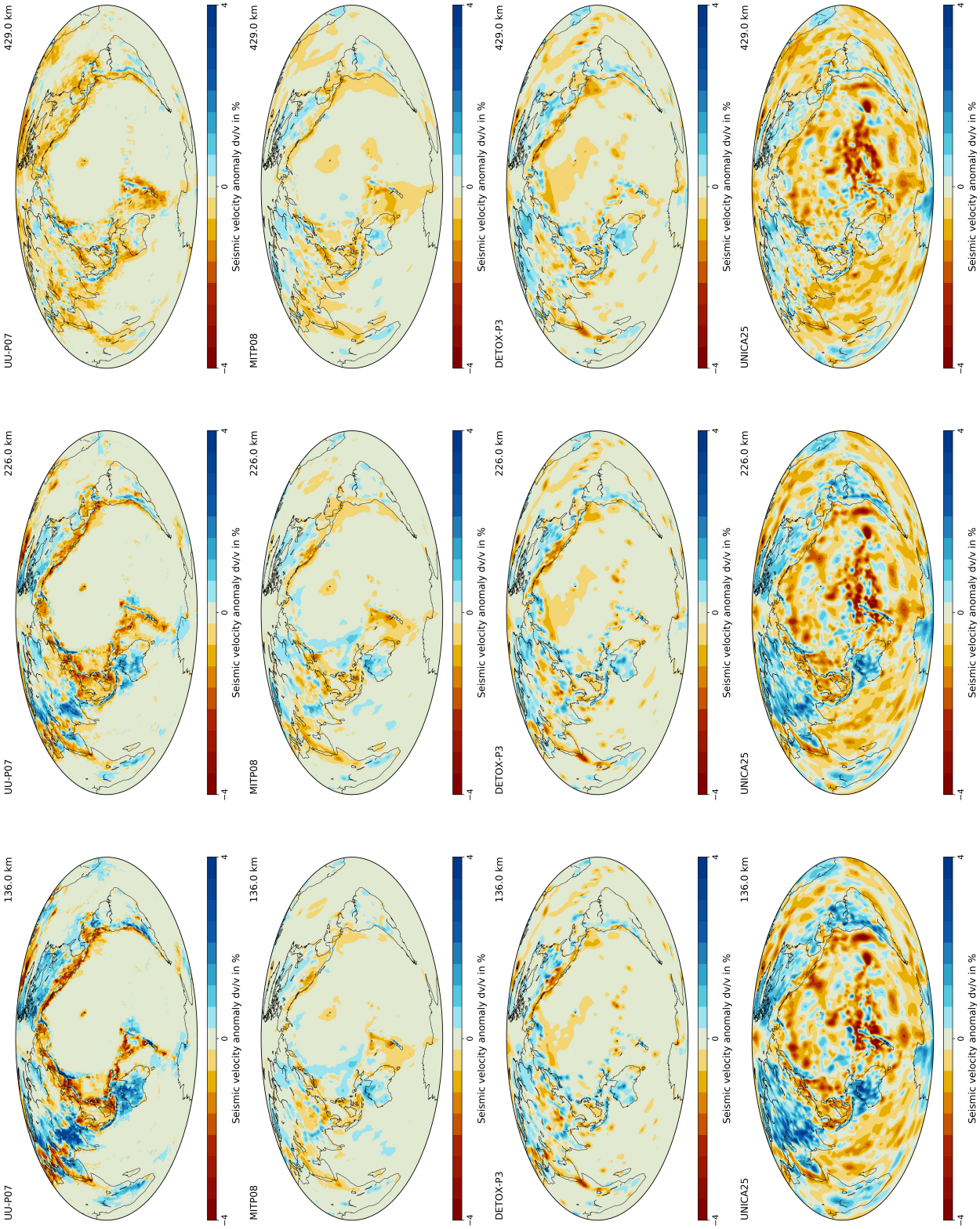

Figure S23: Comparison of Models UU-P07, MITP08, DETOX-P3 with UNICA25. This plot was generated by Submachine (Hosseini et al., 2018).

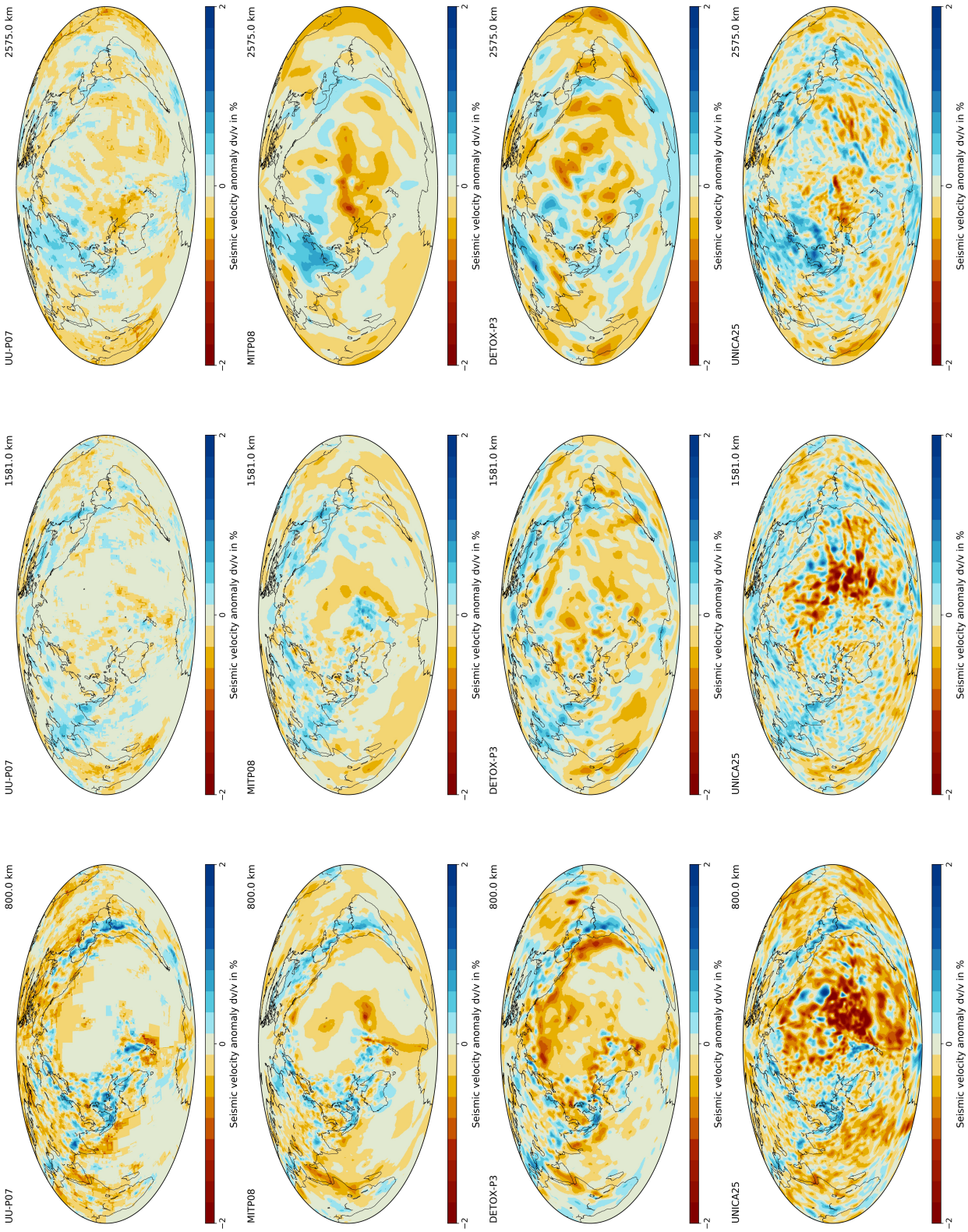

Figure S24: Comparison of Models UU-P07, MITP08, DETOX-P3 with UNICA25. This plot was generated by Submachine (Hosseini et al., 2018).

References

[1] Y. Aizawa, A. Yoneda, T. Katsura, E. Ito, T. Saito, and I. Suzuki. Temperature derivatives of elastic moduli of $MgSiO_3$ perovskite. *Geophys. Res. Lett.*, 31:L01602, 2004.

[2] K. Hosseini, K.J. Matthews, K. Sigloch, G.E. Shepard, M. Domeier, and M. Tseknistrenko. Submachine: Web-based tools for exploring seismic tomography and other models of Earths deep interior. *Geochem. Geophys. Geosys.*, 19, 2018.

[3] S. Karato. Importance of anelasticity in the interpretation of seismic tomography. *Geophys. Res. Lett.*, 20:1623–1626, 1993.

[4] B.B. Karki, R.M. Wentzcovitch, S. de Gironcoli, and S. Baroni. First principles determination of elastic anistropy and wave velocities of MgO at lower mantle conditions. *Science*, 286:1705–1707, 1999.

[5] G. Nolet, S. Karato, and R. Montelli. Plume fluxes from seismic tomography. *Earth Planet. Sci. Lett.*, 248:685–699, 2006.

[6] R.M. Wentzcovitch, B.B. Karki, M. Cococcioni, and S. de Gironcoli. Thermoelastic properties of $MgSiO_3$-perovskite: insights on the nature of the Earth's lower mantle. *Phys. Rev. Lett.*, 92:018501 1–4, 2004.